



Deposited via The University of Leeds.

White Rose Research Online URL for this paper:

<https://eprints.whiterose.ac.uk/id/eprint/201862/>

Version: Accepted Version

Article:

Cao, S., Zhang, L., Mountney, N.P. et al. (2023) Ultra-long-distance transport of aeolian sand: The provenance of an intermontane desert, south-east China. *Sedimentology*. ISSN: 0037-0746

<https://doi.org/10.1111/sed.13106>

© 2023 International Association of Sedimentologists. This is the peer reviewed version of the following article: Cao, S., Zhang, L., Mountney, N.P., Ma, J., Hao, M. and Wang, C. (2023), Ultra-long-distance transport of aeolian sand: The provenance of an intermontane desert, south-east China. *Sedimentology*, which has been published in final form at <https://doi.org/10.1111/sed.13106>. This article may be used for non-commercial purposes in accordance with Wiley Terms and Conditions for Use of Self-Archived Versions. This article may not be enhanced, enriched or otherwise transformed into a derivative work, without express permission from Wiley or by statutory rights under applicable legislation. Copyright notices must not be removed, obscured or modified. The article must be linked to Wiley's version of record on Wiley Online Library and any embedding, framing or otherwise making available the article or pages thereof by third parties from platforms, services and websites other than Wiley Online Library must be prohibited.

Reuse

Items deposited in White Rose Research Online are protected by copyright, with all rights reserved unless indicated otherwise. They may be downloaded and/or printed for private study, or other acts as permitted by national copyright laws. The publisher or other rights holders may allow further reproduction and re-use of the full text version. This is indicated by the licence information on the White Rose Research Online record for the item.

Takedown

If you consider content in White Rose Research Online to be in breach of UK law, please notify us by emailing eprints@whiterose.ac.uk including the URL of the record and the reason for the withdrawal request.

1 Ultra-long-distance transport of aeolian sand: the
2 provenance of an intermontane desert, SE China

3
4 **Shuo Cao¹, Laiming Zhang¹, Nigel P. Mountney², Jing Ma³, Mingang Hao¹, and**
5 **Chengshan Wang¹**

6
7 *¹State Key Laboratory of Biogeology and Environmental Geology, and School of Earth*
8 *Sciences and Resources, China University of Geosciences (Beijing), Beijing 100083,*
9 *China.*

10 *²Fluvial, Eolian & Shallow-Marine Research Group, School of Earth and Environment,*
11 *The University of Leeds, LS2 9JT, UK.*

12 *³Institute of Mineral Resources Research, China Metallurgical Geology Bureau,*
13 *Beijing 101300, China.*

14
15
16 **ABSTRACT**

17 Intermontane deserts are an important type of arid-climate sedimentary system.
18 Although rare at present, the sedimentary records of intermontane deserts reveal their
19 widespread development in past greenhouse periods, and they might develop in the near
20 future in response to ongoing global warming. Determination of the provenance of sand
21 supplied for the construction of intermontane deserts is important to gain improved
22 understanding of the potential impact of future climate on environmental evolution in
23 arid and semi-arid regions. During the Cretaceous, a typical intermontane desert
24 developed in the Xinjiang Basin, southeast China. In this study, the origin, spatial
25 variability, and transport pathways of both aeolian and alluvial-fluvial sediments in the

26 Xinjiang intermontane desert are investigated by analyses of bulk-rock petrography and
27 detrital-zircon U-Pb geochronology. Our results demonstrate that the sand in the
28 Xinjiang intermontane desert succession was mainly of extraneous origin and wind-
29 derived. The nearby South China Block and South China Magmatic Belt were primary
30 sources, and the 1000 km-distant western margin of Yangtze Block was an important
31 secondary source. During the Late Cretaceous, the westerlies were stronger in the
32 northern than in the southern hemisphere with doubled wind speeds. In such a climatic
33 context, our results suggest that the ultra-long-distance aeolian sediment transport was
34 likely further enabled by two factors: (i) the strengthening of intermittent westerly
35 winds during short-lived glacial episodes; (ii) the presence of a low-relief corridor that
36 served as a transport pathway from source to sink.

37 Keywords: intermontane desert; provenance analysis; U-Pb zircon ages; sand supply
38 mechanism; ultra-long-distance transportation

39

40 **INTRODUCTION**

41 At present, approximately 30% of the Earth's land surface is covered by climatic
42 deserts, making them one of the most important terrestrial sedimentary environments
43 (Brookfield and Silvestro, 2010; Mountney, 2006; Rodríguez-López et al., 2014). On
44 the basis of geomorphic features, these dryland regions can be divided into shield-
45 platform deserts and intermontane deserts (Cooke et al., 1993; Whitford and Duval,
46 2019); the latter type is the subject of this study. Shield-platform deserts develop across
47 tablelands and basin lowlands bordered by ancient mountains. This type of desert is

48 widespread today and their preserved successions are widely identified in the ancient
49 rock record (e.g., Rodríguez-López et al., 2014; Rittner et al., 2016; Dickinson and
50 Gehrels, 2003). In contrast, intermontane deserts develop and accumulate principally
51 in valleys and structural depressions that are typically confined by geologically younger
52 mountain ranges (Cooke et al., 1993; Whitford and Duval, 2019). Today, relatively few
53 intermontane deserts are developed; notable examples are present in the Basin and
54 Range Province of the Western United States. Typical intermontane deserts tend to be
55 relatively less sandy, and are commonly called steppe-deserts, such as in Patagonia.
56 Despite being of limited number and extent today, the sedimentary records of preserved
57 examples of intermontane deserts are many, and their development was apparently
58 especially widespread during past greenhouse periods (Barbolini et al., 2020;
59 Brookfield, 1980; Cao et al., 2020; Chen et al., 2008; Jiang et al., 1999; Jiao et al., 2020;
60 Li et al., 2018b; Walker et al., 2002; Yu et al., 2020). For example, many sand-prone
61 intermontane deserts are known to have developed in Asia during greenhouse
62 conditions during the Cretaceous in response to worldwide desertification (Cao et al.,
63 2020; Chen et al., 2019; Li et al., 2018a; Li et al., 2018b; Wu et al., 2017; Wu et al.,
64 2018; Yu et al., 2020).

65 In the near future, as mean global atmospheric CO₂ concentrations continue to rise,
66 it is predicted that the Earth may enter a prolonged greenhouse state, similar to that
67 experienced during the Cretaceous (Caesar et al., 2013; Intergovernmental Panel on
68 Climate, 2014). Given that the onset of desertification is markedly influenced by
69 climatic change (Brookfield and Silvestro, 2010; Mountney, 2006), it is important to

70 assess how and where intermontane deserts might begin to develop in the near future.
71 This study addresses this challenge by examining sedimentary evidence to reveal the
72 mechanisms of formation a Cretaceous intermontane desert succession. Results of this
73 study are valuable for forecasting the potential development of intermontane deserts in
74 the near future.

75 Assessment of the provenance of sediment (i.e., sediment sources and transport
76 pathways) is essential for understanding the processes of aeolian sediment transport and
77 deposition, and for assessing the sediment state of an aeolian system (Du et al., 2018;
78 Kocurek and Lancaster, 1999; Muhs et al., 2017; Williams, 2015). Provenance analysis
79 provides valuable information to support further sedimentological, geomorphological,
80 and palaeoclimatological studies (Jiang and Yang, 2019). Determination of the
81 provenance of desert sediments has been a major focus of numerous recent aeolian
82 studies (e.g., Lancaster et al., 2013; Zhang et al., 2020), and has been important to
83 improve understanding of how and why large accumulations of aeolian sediments are
84 developed and preserved (Bertolini et al., 2020; Dickinson and Gehrels, 2003, 2009).
85 Previous studies of aeolian sediment provenance have hitherto mainly been conducted
86 for shield-platform deserts. Such studies have demonstrated that the aeolian deposits
87 typically comprise both endogenous sands generated by wind erosion of surrounding
88 local bedrock (e.g., parts of the Sahara Desert) and exogenous sands supplied by
89 external or adjacent rivers (e.g., the Namib Desert) (Garzanti et al., 2014; Zhang et al.,
90 2020; Bertolini et al., 2020). However, the provenance of sand supply to intermontane
91 deserts remains relatively poorly understood.

92 The aim of this paper is to reconstruct sediment transportation to (and within) an
93 intermontane desert developed during a greenhouse period. Recently, a Mid-Late
94 Cretaceous intermontane desert has been identified in the Xinjiang Basin, Southeastern
95 China (Wu et al., 2018a; Jiang et al., 2008) (Fig. 1). Within the preserved succession of
96 this intermontane desert system, analyses of indicators of palaeowind and subaqueous
97 palaeocurrents have demonstrated that the formative aeolian and fluvial flows were
98 oriented in opposing directions (Cao et al., 2020). This partitioning of wind- and river-
99 derived sediments is conducive to studying aeolian sand supply. In this study, the origin,
100 spatial variability, and transport pathways of both aeolian and alluvial-fluvial sediments
101 in the Xinjiang intermontane desert are investigated by combining bulk-petrography
102 analyses and detrital-zircon U-Pb geochronology. Results additionally provide
103 constraints on palaeoclimate and palaeogeography.

104

105 **GEOLOGICAL SETTING**

106 The South China Block (SCB) comprises the Yangtze Block (YB) to the northwest
107 and the Cathaysia Block (CB) to the southeast (Fig. 1); each of these blocks has
108 distinctive crustal ages and tectonic histories (Yan et al., 2011; Duan et al., 2011). In
109 response to Cretaceous lithospheric extension in the SCB, a series of terrestrial rifted
110 basins that collectively represent the Late Mesozoic Basin and Range System developed
111 between the YB and the CB (Wang and Shu, 2012; Chen et al., 2017; Shu et al., 2009).
112 During the Mid-Late Cretaceous, many deserts developed in these intermontane basins
113 under the influence of a subtropical high-pressure belt (Cao et al., 2020; Chen et al.,

114 2019; Chen et al., 2008; Jiang et al., 1999; Li et al., 2018a; Li et al., 2018b; Wu et al.,
115 2017; Wu et al., 2018; Yu et al., 2021a). As a representative of these intermontane basins,
116 the Xinjiang Basin accumulated a >6000 m-thick succession of red beds (Guo et al.,
117 2013). Within the overall red-bed succession, a >400 m-thick sequence of aeolian-
118 dominated strata comprising dune-set, interdune, and sandsheet architectural elements
119 has been recognized; this has been interpreted as the sedimentary record of an
120 intermontane desert (Cao et al., 2020; Wu et al., 2018a).

121 The Xinjiang Basin covers an area of over 3600 km²; this elongate basin is 130
122 km E-W and 30 km N-S (Cao et al., 2020). The basin is located in the central part of
123 the Ganhang tectonic belt, which is itself located at the junction of the YB and the CB
124 (Fig. 1B). The basin is fringed by the Jiangnan Orogen (JNO) to the northwest and by
125 the South China Magmatic Belt (SCMB) to the southeast; these two uplifted regions
126 were the closest potential substantial sediment sources that may have contributed to the
127 basin fill, and each of them has distinctive magmatic rock ages (Cawood et al., 2018).
128 The JNO is characterized by an abundant population of relatively younger zircons
129 (~700-800 Ma), and two populations of older zircons (~1550-2000 Ma and ~2300-2600
130 Ma) (Li et al., 2018). By contrast, the SCMB is characterized by abundant zircons with
131 an age of ~80-300 Ma (Yan et al., 2011).

132 From bottom to top, the stratigraphic units of the Xinjiang Basin are the Lower
133 Cretaceous Huobashan Group and the Upper Cretaceous Guifeng Group (Xi et al., 2019)
134 (Fig. 2). Due to an absence of both age-diagnostic fossils and of datable volcanic ash
135 layers, there are no direct absolute age constraints for the overall succession. Deposits

136 of the Guifeng Group have been interpreted as the preserved succession of a typical
137 intermontane desert (Cao et al., 2020). It is subdivided into the basal Hekou Formation
138 (K₂h), the middle Tangbian Formation (K₂t), and the topmost Lianhe Formation (K₂lh).
139 The Hekou and Lianhe formations (each 2000–3000 m thick) are mainly composed of
140 thick- to very thick-bedded purple-red conglomerates and sandy conglomerates with a
141 lesser amount of thin- to medium-bedded sandstones, siltstones, and mudstones. These
142 formations represent alluvial-fan and braided-stream palaeoenvironments (Guo et al.,
143 2013). Between the above-mentioned two formations, the middle Tangbian Formation
144 (~500 m thick) is characterized by brick-red, fine- to medium-grained, well-sorted
145 massive quartz sandstones with well-developed large-scale (ca. 5-10 m thick) simple
146 sets that are internally characterized by high-angle-inclined cross-bedding. Before
147 correction to negate any component of tectonic tilt, the maximum foreset dip angles are
148 ~35° to 42° ; following restoration, the maximum foreset dip angles are ~29° to
149 36° . These deposits have been interpreted to be of aeolian dune origin (Chen et al.,
150 2016; Wu et al., 2018a).

151 According to the previous studies of aeolian deposits in the Sichuan Basin (Jiang
152 et al., 1999) and the Jiangnan Basin (Yu et al., 2021b) to the west of the Xinjing Basin
153 (Fig. 1), the regional wind patterns in the SCB were dominated by westerlies during the
154 Mid-Late Cretaceous: the dominant prevailing wind blew along the elongate axis of the
155 Xinjiang Basin (Cao et al., 2020; Wu et al., 2018). The sedimentary record of west-to-
156 east aeolian sand transport is recorded by the overall orientation of foresets within
157 cross-bedded aeolian dune architectural elements in the Tanbian succession (Fig. 1).

158 These dip-azimuths of the foresets of the aeolian dune-set deposits are indicators of the
159 palaeowind direction because Cao et al. (2020) and Wu et al. (2018) have demonstrated
160 that the formative dunes were perfectly transverse (*sensu* Rubin and Carter, 2006)
161 barchanoid dunes. The mean foreset dip-azimuths of cross-beds of these perfectly
162 transverse dunes are distributed unimodally (see Supplementary S1 for details). Based
163 on the above observations, the average wind direction archived by the mean foreset-dip
164 azimuths is oriented to the ENE (vector mean= 074°) (Fig. 1 and Fig. S2). Thus, the
165 mean sediment transport in the Xinjiang intermontane desert was affected by westerlies
166 during the Mid-Late Cretaceous (Fig. S2). By contrast, the palaeocurrent directions
167 reconstructed from cross-bedded foresets of alluvial-fluvial architectural elements
168 suggest an overall east-to-west (vector mean= 278°) aqueous sediment transport in the
169 Xinjiang Basin (Fig. 1) (Cao et al., 2020; Wu et al., 2018a).

170

171 **DATA AND METHODS**

172 **Sediment Samples**

173 For this study, 14 sandstone samples were collected along a west-to-east transect
174 across the Xinjiang Basin (Fig. 1): four samples of fluvial-alluvial affinity were
175 collected from the Hekou and Lianhe formations; ten samples of aeolian affinity were
176 collected from the Tangbian Formation. Five of the 10 aeolian samples were from
177 deposits of aeolian barchan and transverse dune origin and these were collected from
178 the intermontane desert-centre setting; the other 5 aeolian samples were collected from
179 the desert-margin setting, and are of barchan dune (2), dry interdune (2), and sandsheet

180 (1) origin (see Table S1 for detail information of location and dune type of each sample).

181

182 **Palaeocurrent Indicators**

183 One-thousand-five-hundred-and-thirty dip-azimuth readings were measured from
184 366 separate aeolian dune sets that are themselves interpreted to be the preserved
185 products of perfectly transverse (barchanoid) aeolian bedforms (Cao et al., 2020; cf.
186 Rubin & Carter, 2006). These data have been used to reconstruct palaeo-bedform
187 migration directions, and thereby palaeowind direction. The mean reconstructed wind
188 direction was ENE (vector mean= 074°), which reflects the influence of dominant
189 westerlies (Fig. 1).

190 For the strata of alluvial-fluvial origin, fifty-four palaeocurrent readings were
191 measured from imbricated clasts present in 10 separate sets. In addition, 48 readings
192 were measured from the orientation of elongate trough axes of trough cross-beddings
193 seen in plan view present in 11 separate sets. The mean vector orientation of these 102
194 readings is 278° , and the spread in the data indicates that the palaeocurrent directions
195 ranged from NW to SW, with flow away from the surrounding mountains toward the
196 centre of the intermontane basin (Fig. 1) (Cao et al., 2020; Wu et al., 2018a).

197

198 **Petrography**

199 Bulk sand samples were impregnated with araldite epoxy, cut into standard thin
200 sections, and analyzed by counting at least 300 points (grains) under the petrographic
201 microscope. Following the Gazzi-Dickinson point-counting method, every individually

202 analyzed grain was checked to ensure that it was larger than 62.5 μm (cf. Ingersoll et
203 al., 1984; Dickinson, 1985). Sandstone classification has been undertaken based on the
204 relative abundance of three main framework components: quartz (Q), feldspars (F), and
205 lithic fragments (L), and is displayed on a standard Q-F-L ternary diagram (cf. Garzanti,
206 2019). For lithotype naming, as per convention, the less abundant component is stated
207 first, then the more abundant ones (e.g., litho-feldspatho-quartzose composition
208 translates into $Q > F > L > 10\% \text{ QFL}$).

209 Aeolian sediments commonly exhibit distinctive grain size, shape, and sorting
210 characteristics. Many aeolian sandstones are characterized by very-fine to medium sand
211 that is well or very-well sorted, and with grains that are rounded to subangular
212 (Lindholm, 2012; Mountney, 2006). The majority of grains have a thin coating (surface
213 veneer) of iron oxides. Quartz is commonly dominant, and aeolian sandstones mostly
214 plot in the quartzose (Q), feldspatho-quartzose (FQ), litho-feldspatho-quartzose (IFQ),
215 feldspatho-litho-quartzose (fLQ), and litho-quartzose (LQ) fields (Muhs, 2004;
216 Garzanti, 2019). In contrast, alluvial-fluvial sediments range from extremely coarse
217 conglomerates to fine muds. In these sediments, the sand components are typically
218 characterized by very-fine to coarse sand grains that are poorly sorted, many of which
219 are subangular to angular (Chen et al., 2017). Alluvial-fluvial sandstones mostly plot in
220 the quartzo-litho-feldspathic (qLF), quartzo-feldspatho-lithic (qFL), feldspatho-
221 quartzo-lithic (fQL), feldspatho-litho-quartzose (fLQ), litho-feldspatho-quartzose
222 (IFQ), and litho-quartzo-feldspathic (lQF) fields (Lugli et al., 2007).

223

224 **Detrital Geochronology**

225 In this study, 6 sandstone samples were analyzed by detrital-zircon U-Pb
226 geochronology. Each sample (2 kg) was crushed to 40-60 mesh (i.e., 250-380 μm grain
227 diameter). Conventional magnetic and heavy liquid separation techniques were then
228 used to extract a zircon-rich heavy mineral concentrate (Du et al., 2015). For each
229 sample, a total of 250-300 zircon grains were hand-picked under a binocular
230 microscope. Zircon grains were mounted in epoxy resin and polished to about half their
231 thickness for analysis. Cathodoluminescence (CL) images were taken for all the
232 samples, using a CAMECA electron microprobe, to identify internal textures and
233 choose potential target sites for U-Pb analyses.

234 For each sample, 100 zircons were randomly selected and analyzed. Zircon U-Pb
235 analyses were carried out following the laser ablation inductively coupled plasma mass
236 spectrometry (LA-ICP-MS) methodology in a microanalysis laboratory affiliated with
237 the State Key Laboratory of Geological Processes and Mineral Resources, China
238 University of Geosciences, Beijing. The laser sampling was performed using a
239 Coherent GeoLasPro 193 nm system. A Thermo Fisher X-Series 2 ICP-MS instrument
240 was used to acquire ion signal intensities. All data were acquired from zircon samples
241 in a single spot ablation mode with a spot size of 32 μm and frequency of 6 Hz.
242 Reference and internal zircon standards 91500 and SRM610 were used for instrument
243 calibration, respectively. Off-line selection and integration of background and analyte
244 signals, as well as time-drift correction and quantitative calibration for trace element
245 analyses and U-Pb dating, were performed using ICPMSDataCal (Wu et al., 2018b).

246 Common lead was corrected using the LA-ICP-MS common lead correction
247 procedure (ver. 3.15) (Andersen, 2002). Isoplot/Ex (version 4.15) computer software
248 was used for data reduction and to produce the concordia diagrams with 1σ uncertainty
249 (Ludwig, 2003). U-Pb ages from the zircon grains were calculated by one of two
250 systems: $^{207}\text{Pb}/^{206}\text{Pb}$ age for older (>1 Ga) zircons and $^{206}\text{Pb}/^{238}\text{U}$ for younger ones.
251 Ages that have more than $\pm 10\%$ discordance were excluded from the subsequent
252 analysis.

253

254 **RESULTS**

255 **Sandstone Petrography**

256 All the aeolian sandstone samples analysed are quartz-rich and characterized by
257 fine- to medium-grained, moderate to well-sorted, subrounded to subangular grains.
258 Quartz clasts are the most abundant constituent in these samples, constituting 57%–81%
259 (average 75%) of the framework. Predominant monocrystalline quartz grains exhibit
260 undulatory or blocky extinction; they account for 71% of the total quartz grains, on
261 average (Fig. 3). The majority of the feldspar clasts are plagioclase (80%), with a lesser
262 amount of potassium feldspar clasts (20%). In contrast to the aeolian sandstones, the
263 sandstones of alluvial-fluvial origin mainly consist of medium- to coarse-grained,
264 poorly sorted, subangular to angular grains. Of these samples, three contain ~44% lithic
265 fragments, ~52% quartz clasts, and ~4% feldspar clasts, on average; the remaining
266 sample contains ~25% lithic fragments, ~49% quartz clasts, and ~26% feldspar clasts
267 (Fig. 3).

268 In the QFL diagram (Fig. 3E), all sandstone samples of aeolian origin plot in the
269 litho-quartzose field, although one sample has a relatively higher proportion of lithic
270 components. For the sandstone samples of alluvial-fluvial origin, two plot in the litho-
271 quartzose field, one in the quartzo-lithic field, and one plots at the boundary of the litho-
272 feldspatho-quartzose (lFQ) and feldspatho-litho-quartzose (fLQ) fields (Fig. 3E).

273

274 **Detrital Zircon Morphology**

275 The zircons in aeolian samples YT-03 and YT-08 (desert-centre setting) are 80–
276 120 μm in length with aspect ratios between 1:1 and 2:1. They are dominantly
277 moderately to well-sorted, rounded to subrounded grains that are subspherical to
278 elongate in shape, and brown, reddish-brown, or grey in colour (Fig. 4). The zircons in
279 aeolian samples YT-07 and YT-13 (desert-margin setting) are 100–150 μm in length
280 with aspect ratios between 1.5:1 and 3:1. They mainly share the same characteristics as
281 the desert-centre zircons, although ~25% of them are prismatic, sub-angular fragmented,
282 and relatively larger (120-150 μm in length) (Fig. 4).

283 Compared to those in the samples of aeolian origin, the zircons in the samples of
284 alluvial-fluvial origin (YT-12 and YT-14) have a higher proportion of fragmented and
285 euhedral grains, which account for ~88% of all the grains. These zircons are larger (50–
286 200 μm in length), have aspect ratios between 2:1 and 4:1, are mainly subangular to
287 angular, and are moderately or poorly sorted (Fig. 4).

288 All the zircon grains, from samples of both aeolian and alluvial-fluvial origin, vary
289 from subspherical to elongate in shape and exhibit varied colours. There is no

290 systematic correlation among shape, colour, angularity, and U-Pb ages.

291

292 **Detrital Zircon Geochronology**

293 The Th/U ratios of zircons generally reflect their origins (Maas et al., 1992). The
294 metamorphic zircons typically have low Th/U ratios (<0.1), whereas magmatic zircons
295 mostly have higher Th/U ratios (0.2 to 1.0) (Kinny et al., 1990). In this study,
296 approximately 95% zircons from the Xinjiang Basin have high Th/U ratios (>0.2) (Fig.
297 S3), which suggest magmatic origins.

298 In this study, for each sample, 84–95 grains of the 100 grains counted were
299 evaluated to be valid. A total of 367 and 172 zircon grain U-Pb ages were obtained from
300 the sandstone samples of aeolian and alluvial-fluvial origin, respectively. All valid
301 results are plotted on the Concordia curve and give high concordant ages (Fig. 5).
302 Figure 6 shows the relative age-probability plots and the spectra of U-Pb ages for all
303 the samples. The ages of all the samples could be grouped into seven clusters: 98–217
304 Ma, 220–323 Ma, 328–482 Ma, 503–722 Ma, 732–1386 Ma, 1426–2174 Ma, and
305 2210–2701 Ma. For each sample, the proportions of age clusters are different. In
306 addition to the clusters referred to above, two older grain populations with ages of 2834
307 Ma and 3240 Ma were identified in sample YT-07 (Fig. 5).

308 The seven main U-Pb age clusters are recognized in all the aeolian samples. The
309 4th cluster (503–722 Ma) is exclusive to the aeolian samples, and the 5th cluster (732–
310 1386 Ma) represents the largest proportion (30-40%). However, the proportions of age
311 clusters are different between samples from the central and the marginal settings of the

312 intermontane desert (Fig. 6). The proportion of the 1st cluster (98–217 Ma) is lower in
313 the desert-centre setting (3–10%) than that in the desert-margin setting (16%). The 6th
314 and 7th clusters (1426–2174 Ma and 2210–2701 Ma) together occupy a higher
315 proportion in the desert-centre setting (31–43%) than those in the desert-margin setting
316 (16–21%). For the sandstone samples of alluvial-fluvial origin, six age clusters are
317 recognized in sample YT-12 and five age clusters are recognized in sample YT-14 (Fig.
318 6). As the highest age population, the 1st cluster (98–217 Ma) accounts for 61–68%.
319 The 5th cluster (732–1386 Ma) is the second-highest population and accounts for 14–
320 17%, which is less than those of the sandstone samples of aeolian origin. For the other
321 four age clusters, each of them accounts for <8%, which are excluded from detrital
322 zircon geochronology analysis for the alluvial-fluvial samples (Gehrels, 2012; Yan et
323 al., 2011).

324

325 **Youngest Detrital Zircon Ages**

326 Due to the absence of age-diagnostic fossils and volcanic layers, the age of the
327 intermontane desert is poorly constrained. The zircon U-Pb geochronology could
328 provide a constraint on maximum depositional age (MDA) for each sample. Table 1
329 presents five MDA candidates for each sample, and the chosen MDA in this study is
330 constrained by YC1 σ (2+). The Guifeng Group, which consists of the Hekou, Tangbian,
331 and Lianhe formations, yields a MDA of ca. 109.5–99.5 Ma. Therefore, the maximum
332 depositional age (i.e., ca. 109.5–99.5 Ma) reveals that the intermontane desert formed
333 no earlier than the mid-Cretaceous. Our age constraint is consistent with Li et al. (2019)

334 who suggested that the Guifeng Group is Cenomanian-Santonian in age.

335

336 **DISCUSSION**

337 **Aeolian and alluvial-fluvial system interaction in intermontane deserts**

338 Wu et al. (2018) and Cao et al. (2020) studied the sedimentary characteristics and
339 internal architecture of aeolian and alluvial-fluvial deposits of the Guifeng Group in the
340 Xinjiang Basin. As an outcome of this work, these researchers identified the
341 intermontane desert environment, although the provenance of the aeolian sediments
342 was not considered. Investigation of the provenance of the aeolian sediments might
343 assist in the interpretation of the interaction between aeolian and alluvial-fluvial
344 sediments in this specific case and for intermontane desert successions more generally.

345 Climatic deserts are governed dominantly by two competing agents of sediment
346 transport, wind and water (Dickinson and Gehrels, 2009, 2003). Wind-supplied deserts
347 commonly derive sediment from both endogenous and exogenous sources: (i)
348 surrounding bedrock and loose sediment that originally carried by wind or water; and
349 (ii) more distant sediments. Water-supplied deserts commonly derive sediment from (i)
350 exogenous sands that are external but adjacent to the desert system, and (ii) endogenous
351 sands that are entirely within the confines of the desert system (Pastore et al., 2021; Zhu
352 et al., 2014).

353 For the Xinjiang intermontane desert, the distribution of the detrital zircon U-Pb
354 ages of the sediments of alluvial-fluvial origin is unimodal (i.e., 98–217 Ma), which
355 differs from the multi-modal age distributions of the sediments of aeolian origin (Fig.

356 7). For the desert-centre setting, the peak of the 1st cluster (i.e., 98–217 Ma) in the
357 aeolian samples is different from that of the alluvial-fluvial samples (Fig. 5).
358 Sedimentary facies analyses by Wu et al. (2018) and Cao et al. (2020) also found no
359 evidence to indicate deposition via aqueous flows in deposits of the desert-centre setting.
360 Thus, available evidence demonstrates that all the sediments from the desert-centre
361 setting are of aeolian origin.

362 The interaction between fluvial sediment supply and subsequent partial aeolian
363 reworking of that supply is documented at the periphery of several shield-platform
364 deserts (Pastore et al., 2021). In the Xinjiang intermontane desert, the sediments in the
365 desert-margin setting are also a mixture of both wind- and river-transported sediments.
366 The detrital zircons from the desert-margin setting are variably rounded to angular, and
367 have characteristics of transport via both aeolian and alluvial-fluvial processes (Fig. 4).
368 In the Xinjiang intermontane desert, the 1st cluster (98–217 Ma) is the most and least
369 abundant component for the river- and wind-transported sandstones, respectively. For
370 the desert-margin samples, the percentage of the 1st cluster (98–217 Ma) is more
371 abundant than the central-desert samples (Fig. 6). The increase in the proportion of the
372 1st cluster is influenced by the input of river-transported sediments. In addition, there is
373 one aeolian sandstone sample (JXY-21) from the desert-margin setting that contains
374 more lithics component, which is similar to the alluvial-fluvial samples (Fig. 3).

375 Based on the above discussion, we propose that the Xinjiang intermontane desert-
376 centre region was entirely controlled by aeolian sedimentary processes, which is similar
377 to much of the present-day Sahara Desert (Pastore et al., 2021). By contrast, the desert

378 margin was controlled by both aeolian and alluvial-fluvial processes, with preserved
379 deposits of both aeolian and alluvial-fluvial facies, similar to parts of the Taklamakan
380 Desert (Rittner et al., 2016). Pastore et al. (2021) suggested that, during the hyperarid
381 episodes, river activity in deserts might be weakened to the extent that the fluvial
382 contribution to and interaction with aeolian dune fields becomes negligible. During the
383 Mid-Late Cretaceous, the intermontane deserts generally developed under hyperarid-
384 arid climates in China (Cao et al., 2020). We, therefore, suggest that aeolian and
385 alluvial-fluvial interactions were likely be confined solely to the marginal areas of this
386 intermontane desert.

387

388 **Provenance Analysis of the Xinjiang intermontane desert**

389 *Source areas of the alluvial-fluvial sandstones*

390 Sandstones of the Hekou and Lianhe formations of alluvial-fluvial origin consist
391 of medium-coarse grained, poorly sorted, and subangular to angular grains, and contain
392 a relatively high content of feldspars and lithic fragments. In addition, their zircon U-
393 Pb ages yield a distinct unimodal distribution (Fig. 5). These observations indicate a
394 relatively proximal source area and a rapid accumulation rate. The palaeocurrent
395 indicators reveal that the sediments were mainly transported from the southeast to the
396 northwest (Fig. 1) (Chen et al., 2016).

397 These alluvial-fluvial sandstones are dominantly composed of Cretaceous (98–145
398 Ma) and Jurassic (145–197 Ma) zircons. These zircons are similar to those of the Upper
399 Cretaceous sandstones in the Hengyang Basin (Yan et al., 2011). The Jurassic zircon U-

400 Pb ages are consistent with the ages of the Yanshanian granites in the SCB (Fig. 7). The
401 Yanshanian magmatism commenced at ca. 190 Ma in the inland region; it propagated
402 from the centre of the SCB and continued in the broad inland region until ca. 150 Ma
403 (Li and Li, 2007). The Cretaceous granitic intrusive rocks (98–145 Ma) in this region
404 occur mainly along the northeast part of the zone between the YB and the CB, and the
405 coastal region (Fig. 7) (Li, 2000). Thus, the nearby SCB and SCMB were the most
406 likely source areas of the alluvial-fluvial sandstones in the Xinjiang intermontane desert.

407 *Source areas of the aeolian sandstones*

408 Sandstones of the Tangbian Formation of aeolian origin are quartz-rich, finer
409 grained and are better sorted and more rounded. They have a wide range of detrital
410 zircon U-Pb ages (Fig. 5). These sediments were likely derived from multiple source
411 areas and underwent long-distant transportation. The most abundant detrital zircon age
412 cluster in the aeolian sandstones is 732–1386 Ma (from Neoproterozoic to
413 Mesoproterozoic). The nearest JNO, a ~970–820 Ma Rodinia margin accretionary belt,
414 is characterized by widely exposed Neoproterozoic basement rocks (Fig. 1). Moreover,
415 ~1550–2000 Ma and ~2300–2600 Ma age populations are common in the JNO (Wang
416 and Zhou, 2012; Li et al., 2018). These three age populations exhibit a perfect match
417 with all the aeolian samples. Therefore, we suggest that the JNO is one of the main
418 sediment sources (Fig. 7).

419 The detrital zircon age clusters of 98–217 Ma, 220–323 Ma, and 328–482 Ma are
420 closely associated with the Yanshanian, Hercynian-Indosinian, and Caledonian
421 movements, respectively (Li et al., 2014). The Cretaceous (98–145 Ma) and Jurassic

422 (145–217 Ma) zircons mainly came from Yanshanian granites (80–205 Ma) in the
423 inland region and southeast coast of the SCMB (Li and Li, 2007). The Late Triassic to
424 mid-Carboniferous (220–323 Ma) zircons were mainly derived from Hercynian-
425 Indosinian granites in the failed rift zone between the YB and the CB (Wang et al.,
426 2007). The Devonian to Ordovician (365–482 Ma) zircons also might have been
427 derived from the SCB. Therefore, the SCB and SCMB were likely to also have been
428 major sediment sources (Fig. 7).

429 A notable age cluster ranges from the Cambrian to Neoproterozoic (503–722 Ma).
430 However, rocks of this age range are generally absent in the SCB, except for the western
431 margin of the SCB (Qi et al., 2023). Moreover, except for contemporaneous (i.e., Late
432 Cretaceous) aeolian deposits in the Jiangnan Basin to the west of the Xinjiang Basin
433 (Yu et al., 2020), almost no zircons with this age range had been recognized in the
434 Upper Cretaceous strata in SCB (Li et al., 2017; Hu et al., 2015). Although it accounts
435 for only ca. 5–6% of all the analyzed grains, this age cluster indicates at least one other
436 sediment source area besides JNO, SCB, and SCMB. Although the JNO contains a few
437 zircons of this age range, if zircons of this age in aeolian samples were all from the JNO,
438 the peak age of ~835 Ma would be particularly obvious in the aeolian samples (Fig. 7).
439 However, the aeolian samples do not have the above age signature. As such, even if the
440 JNO contributed zircons of this age, its contribution would be small; [the majority of the](#)
441 [500-722 Ma cluster of detrital zircons in the aeolian samples must have been provided](#)
442 [by other source areas.](#)

443 Given the reconstructed ENE direction of the palaeowind (Cao et al., 2020), the

444 sediments might have been derived from west-southwest direction to the Xinjiang
445 Basin (see Appendix S1). The western margin of Yangtze Block (W-YB), which
446 comprises abundant Paleozoic sediments with a peak age of ~558 Ma (Duan et al.,
447 2011), is the most likely source area in the westerly direction (Fig. 7). Another peak age
448 of ~942 Ma of W-YB also appears as a secondary peak in aeolian samples, which
449 further supports the hypothesis that the W-YB is the source area. A minor sediment
450 component from further west could have been derived from the Sanjiang Orogen (SJO)
451 and/or the Songpan-Ganzi terrane (SGT) (Fig. 1), since the detrital zircon ages match
452 for all the potential sources (Enkelmann et al., 2007; Wang et al., 2013). In the north,
453 the age peaks of the South and North Qinling Belt (SQB & NQB) and the southern
454 margin of the North China Block (S-NCB) were not compatible with the ages indicated
455 by our aeolian samples (Li et al., 2018). In addition, compared with other detrital
456 zircons in the aeolian samples, the forms of zircons with the age of 503–722 Ma tend
457 to be relatively complete and more angular. These observations may indicate that the
458 aeolian sand originating from the W-YB source was transported as a suspended load to
459 the Xinjiang Basin by the dominant westerlies (Fig. 4 and Fig. S4). Moreover, along
460 the pathway from the W-YB to the Xinjing Basin, the zircons with this age range were
461 also identified in contemporaneous aeolian deposits in the Jiangnan Basin (Fig. 8),
462 which represents secondary peaks with similar contents as the Tangbian Formation in
463 the Xinjiang intermontane desert (Li et al., 2018b; Yu et al., 2020).

464 In summary, the aeolian sandstones in the Xinjiang intermontane desert were
465 derived from multiple sources. The JNO, SCB, and SCMB were the main sources; the

466 W-YB was an important secondary source; and the even more distant SJO and SGT
467 were other potential sources.

468

469 **Ultra-long-Distance Transport of Aeolian Sand**

470 A secondary but significant source area of the sediments in the Xinjiang
471 intermontane desert was the western margin of Yangtze Block (W-YB), which was
472 more than a thousand kilometres away from the Xinjiang Basin. In the Xinjiang Basin,
473 the diameters of the detrital zircons within the relevant age cluster (503–722 Ma) are
474 close to or over 100 μm (Fig. S4). Therefore, our results suggest that sand with a
475 diameter of over 100 μm could be transported over one thousand kilometres by a
476 dominant westerly wind from western China to southeastern China (Fig. 8).

477 It has been shown that fine silt (2-20 μm) can be transported over thousands of
478 kilometres and coarse silt (21-63 μm) can be transported over hundreds of kilometres
479 by winds (Lancaster, 2020). However, previous studies have suggested that very-fine
480 sand (63-125 μm) could only be transported within a few kilometres in short-term
481 suspension or modified saltation by the wind (Tsoar and Pye, 1987; Lancaster, 2020).
482 Hence, the ultra-long-distance aeolian transport of sand grains with a diameter over 100
483 μm requires a wind with a sustained high speed and a favourable geographic
484 arrangement.

485 The equation in Tsoar and Pye (1987) provides important constraints on the
486 relationships of transport distance, wind speed, and particle size for aeolian grains in
487 suspension.

488 $L = \bar{U}^2 \varepsilon / K^2 D^4$

489 where L is transport distance, \bar{U} is mean wind speed, ε is the coefficient of turbulent
490 exchange, $K = \rho_s g / 18 \mu$ (where ρ_s is the grain density; μ is the dynamic viscosity of air;
491 g is gravity), and D is the grain diameter (Tsoar and Pye, 1987). Based on this equation,
492 to transport quartz spheres with a diameter of $\sim 100 \mu\text{m}$ for 1000 km, the minimum wind
493 speed is 24 m/s (i.e., a strong gale).

494 We also evaluate the possibility that the aeolian sediments were transported
495 intermittently along the 1000 km-long sediment transport pathway. For such
496 intermittent sediment transport, the intermittently deposited sediments would likely
497 have been prone to reworking by fluvial erosional processes, and the zircons within the
498 relevant age cluster (503–722 Ma) would be expected to be present along the pathway
499 from the W-YB to the Xinjiang Basin in a decreasing amount. However, there is no
500 other known record of 503–722 Ma zircons along the path from the W-YB to the
501 Xinjing Basin, except for contemporaneous aeolian deposits in the Jiangnan Basin,
502 which also show secondary peaks and similar contents as the Tangbian Formation in
503 the Xinjiang intermontane desert (Li et al., 2018b; Yu et al., 2020). This suggests that
504 the ultra-long-distance aeolian sediment transport could have occurred entirely in
505 suspension as a single event.

506 Currently, the annual mean surface westerly wind speed ranges from only 1 m/s to
507 9 m/s, although the transient speed of the westerly jet can be considerably higher, e.g.,
508 182.5 m/s in the polar front of the jet stream (Schiemann et al., 2009). Neither the low
509 annual mean wind speed nor the strong transient wind speed in tropopause would have

510 been sufficient to transport the $\sim 100 \mu\text{m}$ sand grains over 1000 km. Based on the Late
511 Cretaceous global climate modelling results (Floegel and Wagner, 2006), strong
512 westerlies typically lie between the subtropical highs at 30° . Based on these modelling
513 results, the surface westerlies were considerably stronger in the northern than in the
514 southern hemisphere, with wind speeds up to 11 m/s. This would have strengthened the
515 transportation of $\sim 100 \mu\text{m}$ sand at high altitudes. In addition, Koopmann (1981) argued
516 that the atmospheric circulation and planetary winds were heightened during episodes
517 of dry glacial climate conditions, and that aeolian sand transport would be enhanced
518 during such episodes. For example, the coarse sand grains from the Sahara Desert were
519 transported to the Atlantic Ocean by winds during the Late Cenozoic glacial periods
520 (Koopmann, 1981). The early Late Cretaceous was one of the warmest periods of the
521 Phanerozoic, but the temperature tended to decrease gradually from Turonian to
522 Santonian (Bornemann et al., 2008; O'Brien et al., 2017). According to a compilation
523 of dropstones, tillites, glendonites, eustasy fluctuations, and $\delta^{18}\text{O}$ values, five glacial
524 events during the Mid-Late Cretaceous were recognized in the Albian-Cenomanian
525 boundary, middle and latest Cenomanian, middle Turonian, middle Coniacian, and
526 early Santonian (Bornemann et al., 2008; Chen, 2011; Ladant and Donnadieu, 2016).
527 However, the chronological relationship between the aeolian sandstones in Xinjiang
528 Basin and the Cretaceous glacial events is not rigidly constrained. In addition, the
529 occurrences of striated cobbles in the alluvial facies close to the Xinjiang palaeo-
530 intermontane desert may suggest glacial activity (Jiao et al., 2020). We propose that
531 temporary glacial events might have acted as a trigger for westerlies burst with

532 heightened gale-force wind events capable of transporting sand over an ultra-long
533 distance. And a sustained heightening of wind speed would lead to a relatively high
534 proportion of sand derived from the W-YB being carried to the Xinjiang intermontane
535 desert. In this study, since the aeolian sediments from the W-YB only account for ~6%
536 of the total, we speculate that the westerlies were only intermittently strengthened
537 during the Mid-Late Cretaceous.

538 Compared to silts (dusts) that are carried at high altitudes in suspension, sands are
539 usually carried at lower altitudes and are easily blocked by highlands and mountains.
540 Du et al. (2018) demonstrated that the far-traveled input from the Tarim Basin to the
541 Qaidam Desert is transported through the low areas among the Altyn Tagh Mountains
542 at present in northwestern China. Therefore, a low-relief corridor conducive to aeolian
543 sand transport is also a prerequisite for the ultra-long-distance transportation.
544 According to the Mid-Late Cretaceous palaeogeographic map (Ma et al., 2009; Wang,
545 1985), there was a relatively low-elevation and low-relief corridor between the
546 Southwest China Highland and Palaeo-Qinling-Dabie Mountains. This corridor may
547 have served as a pathway for the ultra-long-distance sand transport from the W-YB to
548 southeastern China (Fig. 8).

549

550 **CONCLUSIONS AND IMPLICATIONS**

551 The results of this study suggest that sand of the Cretaceous Xinjiang intermontane
552 desert was dominantly supplied by aeolian processes, although the desert margin region
553 also received subordinate river-transported sediments. Based on the sandstone

554 petrography, detrital zircon morphology, and U-Pb geochronology, the nearby South
555 China Craton (SCB) and South China Magmatic Belt (SCMB) were the main sediment
556 sources for the Xinjiang intermontane desert. Importantly, the western margin of the
557 Yangtze Block (W-YB) was a notable secondary sediment source; this demonstrates an
558 ultra-long aeolian sand transport pathway of more than 1000 km to the Xinjiang
559 intermontane desert. During the Late Cretaceous, the westerlies were stronger in the
560 northern than in the southern hemisphere, with approximately doubled wind speeds. In
561 such a climatic context, we suggest that the ultra-long aeolian sediment transport was
562 further facilitated by a combination of both (i) the intermittently strengthened westerly
563 winds during short-lived glacial episodes and (ii) the presence of a low-elevation, low-
564 relief corridor that served as a sediment transport route from source to sink across
565 southern China.

566 The results presented herein study also have implications for the development of
567 intermontane deserts more generally. This study demonstrates a plausible relationship
568 between the intermontane deserts and greenhouse climate state. Elevated levels of
569 global atmospheric CO₂ concentration increase the likelihood of development of
570 intermontane deserts during the greenhouse periods. Such conditions might arise in the
571 near future. To further constrain the above issue, more work is needed to investigate the
572 formative mechanisms and the climatic affinities of intermontane deserts in deep time.
573 In addition, previous studies have demonstrated how rainshadow effects caused by the
574 East Asian coastal mountains may have acted to facilitate the development of the Mid-
575 Late Cretaceous intermontane deserts in South China. Nowadays, there are many sand

576 dunes constructed in intermontane basins that border high mountain ranges, notably the
577 Himalaya and Andes. We propose that these sand-dune fields that are currently of
578 modest extent in rainshadow-affected intermontane basins may evolve into larger
579 intermontane deserts in the near future. Additional study, including both monitoring of
580 modern systems and deep-time investigations of successions preserved in the rock
581 record are required.

582

583 **ACKNOWLEDGEMENTS**

584 The authors are grateful to the Editor Dr. Alexander Brasier and Dr. Gonzalo Veiga,
585 and thank Dr. Chihua Wu and two anonymous reviewers for their helpful comments
586 and suggestions on the earlier versions of this manuscript. The authors also thank Rong
587 Chai for discussion. This study was financially supported by the National Natural
588 Science Foundation of China (grants 41888101, 42072116, 42102122, 41790455), the
589 National Key R&D Plan of China (Grant 2018YFE0204204), and the Chinese "111"
590 project (Grant B20011).

591

592 **REFERENCES CITED**

593 **Andersen, T.** (2002) Correction of common lead in U–Pb analyses that do not report
594 ²⁰⁴Pb. *Chemical Geology*, **192**, 59-79.

595 **Barbolini, N., Woutersen, A., Dupont-Nivet, G., Silvestro, D., Tardif, D., Coster,**

596 **P.M.C., Meijer, N., Chang, C., Zhang, H.X., Licht, A., Rydin, C., Koutsodendris,**

597 **A., Han, F., Rohrmann, A., Liu, X.-J., Zhang, Y., Donnadieu, Y., Fluteau, F.,**

598 **Ladant, J.-B., Hir, G.L. and Hoorn, C.** (2020) Cenozoic evolution of the steppe-
599 desert biome in Central Asia. *Science Advances*, **6**, eabb8227.

600 **Bertolini, G., Marques, J.C., Hartley, A.J., Da-Rosa, A.A.S., Scherer, C.M.S., Basei,**
601 **M.A.S. and Frantz, J.C.** (2020) Controls on Early Cretaceous desert sediment
602 provenance in south-west Gondwana, Botucatu Formation (Brazil and Uruguay).
603 *Sedimentology*, **67**, 2672-2690.

604 **Bornemann, A., Norris, R.D., Friedrich, O., Beckmann, B., Schouten, S., Damsté,**
605 **J.S.S., Vogel, J., Hofmann, P. and Wagner, T.** (2008) Isotopic Evidence for Glaciation
606 During the Cretaceous Supergreenhouse. *Science*, **319**, 189-192.

607 **Brookfield, M.E.** (1980) Permian intermontane basin sedimentation in southern
608 Scotland. *Sedimentary Geology*, **27**, 167-194.

609 **Brookfield, M. and Silvestro, S.** (2010) Eolian Systems. In: *Facies Models* (Eds R.W.
610 Dalrymple and N.P. James) 4 edn. Geological Association of Canada, St. John's, Nfld.

611 **Cao, S., Zhang, L., Wang, C., Ma, J., Tan, J. and Zhang, Z.** (2020) Sedimentological
612 characteristics and aeolian architecture of a plausible intermountain erg system in
613 Southeast China during the Late Cretaceous. *GSA Bulletin*, **132**, 2475-2488.

614 **Caesar, J., Palin, E., Liddicoat, S., Lowe, J., Burke, E., Pardaens, A., Sanderson,**
615 **M. and Kahana, R.** (2013) Response of the HadGEM2 Earth System Model to Future
616 Greenhouse Gas Emissions Pathways to the Year 2300. *Journal of Climate*, **26**, 3275-
617 3284.

618 **Cawood, P.A., Zhao, G., Yao, J., Wang, W., Xu, Y. and Wang, Y.** (2018)
619 Reconstructing South China in Phanerozoic and Precambrian supercontinents. *Earth-*

620 *Science Reviews*, **186**, 173-194.

621 **Chen, L., Guo, F., Steel, R.J. and Li, Y.** (2016) Petrography and geochemistry of the
622 Late Cretaceous redbeds in the Gan-Hang Belt, southeast China: implications for
623 provenance, source weathering, and tectonic setting. *International Geology Review*, **58**,
624 1196-1214.

625 **Chen, L., Steel, R.J., Guo, F., Olariu, C. and Gong, C.** (2017) Alluvial fan facies of
626 the Yongchong Basin: Implications for tectonic and paleoclimatic changes during Late
627 Cretaceous in SE China. *Journal of Asian Earth Sciences*, **134**, 37-54.

628 **Chen, Q., Pang, F. and Qu, D.** (2008) Depositional and reservoir characteristics of the
629 Cretaceous Chishan Formation in Subei Basin and their significance. *Marine and*
630 *Petroleum Geology*, **28**, 95-100.

631 **Chen, X., Wang, C. and H, Y.** (2011) Progress in the study of Cretaceous rapid climate
632 change: evidence of glaciation in a greenhouse world. *Geoscience*, **25**, 409-418.

633 **Cooke, R.U., Warren, A. and Goudie, A.S.** (1993) *Desert geomorphology*. CRC Press.

634 **Dickinson, W.R.** (1985) Interpreting Provenance Relations from Detrital Modes of
635 Sandstones. In: *Provenance of Arenites* (Ed G.G. Zuffa), pp. 333-361. Springer
636 Netherlands, Dordrecht.

637 **Dickinson, W.R. and Gehrels, G.E.** (2003) U–Pb ages of detrital zircons from Permian
638 and Jurassic eolian sandstones of the Colorado Plateau, USA: paleogeographic
639 implications. *Sedimentary Geology*, **163**, 29-66.

640 **Dickinson, W.R. and Gehrels, G.E.** (2009) U-Pb ages of detrital zircons in Jurassic
641 eolian and associated sandstones of the Colorado Plateau: Evidence for transcontinental

642 dispersal and intraregional recycling of sediment. *GSA Bulletin*, **121**, 408-433.

643 **Du, S., Wu, Y. and Tan, L.** (2018) Geochemical evidence for the provenance of aeolian
644 deposits in the Qaidam Basin, Tibetan Plateau. *Aeolian Research*, **32**, 60-70.

645 **Du, X., Chen, X., Wang, C., Wei, Y., Li, Y. and Jansa, L.** (2015) Geochemistry and
646 detrital zircon U–Pb dating of Lower Cretaceous volcanoclastics in the Babazhadong
647 section, Northern Tethyan Himalaya: Implications for the breakup of Eastern
648 Gondwana. *Cretaceous Research*, **52**, 127-137.

649 **Duan, L., Meng, Q. R., Zhang, C. L. and Liu, X. M.** (2011) Tracing the position of
650 the South China block in Gondwana: U–Pb ages and Hf isotopes of Devonian detrital
651 zircons. *Gondwana Research*, **19**, 141-149.

652 **Enkelmann, E., Weislogel, A., Ratschbacher, L., Eide, E., Renno, A. and Wooden,**
653 **J.** (2007) How was the Triassic Songpan-Ganzi basin filled? A provenance study.
654 *Tectonics*, **26**, TC4007.

655 **Floegel, S. and Wagner, T.** (2006) Insolation-control on the Late Cretaceous
656 hydrological cycle and tropical African climate—global climate modelling linked to
657 marine climate records. *Palaeogeography, Palaeoclimatology, Palaeoecology*, **235**,
658 288-304.

659 **Garzanti, E.** (2019) Petrographic classification of sand and sandstone. *Earth-Science*
660 *Reviews*, **192**, 545-563.

661 **Garzanti, E., Vermeesch, P., Andò, S., Lustrino, M., Padoan, M. and Vezzoli, G.**
662 (2014) Ultra-long distance littoral transport of Orange sand and provenance of the
663 Skeleton Coast Erg (Namibia). *Marine Geology*, **357**, 25-36.

664 **Gehrels, G.** (2012) Detrital Zircon U-Pb Geochronology: Current Methods and New
665 Opportunities. In: *Tectonics of Sedimentary Basins* (Eds Busby, C.J. and Azor, A.), John
666 Wiley & Sons, Ltd, Chichester, UK, pp. 45-62.

667 **Guo, F., Zhu, Z., Huang, B. and Jiang, Y.** (2013) Cretaceous sedimentary system and
668 their relationship with Danxia landform in Xinjiang Basin, Jiangxi. *Acta*
669 *Sedimentologica Sinica*, **31**, 954-964.

670 **Hasegawa, H., Tada, R., Jiang, X., Suganuma, Y., Imsamut, S., Charusiri, P.,**
671 **Ichinnorov, N. and Khand, Y.** (2012) Drastic shrinking of the Hadley circulation
672 during the mid-Cretaceous Supergreenhouse. *Climate of the Past*, **8**, 1323-1337.

673 **Hu, L., Cawood, P.A., Du, Y., Yang, J. and Jiao, L.** (2015) Late Paleozoic to Early
674 Mesozoic provenance record of Paleo-Pacific subduction beneath south China.
675 *Tectonics*, **34**, 986-1008.

676 **Ingersoll, R.V., Bullard, T.F., Ford, R.L., Grimm, J.P., Pickle, J.D. and Sares, S.W.**
677 (1984) The effect of grain size on detrital modes: a test of the Gazzi-Dickinson point-
678 counting method. *Journal of Sedimentary Research*, **54**, 103-116.

679 **Intergovernmental Panel on Climate, C.** (2014) *Climate Change 2014 – Impacts,*
680 *Adaptation and Vulnerability: Part A: Global and Sectoral Aspects: Working Group II*
681 *Contribution to the IPCC Fifth Assessment Report: Volume 1: Global and Sectoral*
682 *Aspects*. Cambridge University Press, Cambridge.

683 **Jiang, Q. and Yang, X.** (2019) Sedimentological and Geochemical Composition of
684 Aeolian Sediments in the Taklamakan Desert: Implications for Provenance and
685 Sediment Supply Mechanisms. *Journal of Geophysical Research: Earth Surface*, **124**,

686 1217-1237.

687 **Jian, X., Weislogel, A. and Pullen, A.** (2019) Triassic Sedimentary Filling and Closure
688 of the Eastern Paleo-Tethys Ocean: New Insights From Detrital Zircon Geochronology
689 of Songpan-Ganzi, Yidun, and West Qinling Flysch in Eastern Tibet. *Tectonics*, **38**, 767-
690 787.

691 **Jiang, X., Pan, Z. and Fu, Q.** (1999) The variations of palaeowind direction of the
692 Cretaceous desert in the Sichuan Basin and their significance. *Sedimentary Facies and*
693 *Palaeogeography*, **1**, 3-13.

694 **Jiang, X., Pan, Z., Xu, J., Li, X., Xie, G. and Xiao, Z.** (2008) Late Cretaceous aeolian
695 dunes and reconstruction of palaeo-wind belts of the Xinjiang Basin, Jiangxi Province,
696 China. *Palaeogeography, Palaeoclimatology, Palaeoecology*, **257**, 58-66.

697 **Jiao, H., Wu, C., Rodríguez-López, J.P., Sun, X. and Yi, H.** (2020) Late Cretaceous
698 plateau deserts in the South China Block, and Quaternary analogues; sedimentology,
699 dune reconstruction and wind-water interactions. *Marine and Petroleum Geology*, **120**,
700 104504.

701 **Kinny, P.D., Wijbrans, J.R., Froude, D.O., Williams, I.S. and Compston, W.** (1990)
702 Age constraints on the geological evolution of the Narryer Gneiss Complex, Western
703 Australia. *Australian Journal of Earth Sciences*, **37**, 51-69.

704 **Kocurek, G. and Lancaster, N.** (1999) Aeolian system sediment state: theory and
705 Mojave Desert Kelso dune field example. *Sedimentology*, **46**, 505-515.

706 **Koopmann, B.** (1981) Sedimentation von Saharastaub im subtropischen Nordatlantik
707 während der letzten 25.000 Jahre. *"Meteor" Forschungs-Ergebnisse, C*, **35**, 23-59.

708 **Ladant, J. B. and Donnadieu, Y.** (2016) Palaeogeographic regulation of glacial events
709 during the Cretaceous supergreenhouse. *Nature Communications*, **7**, 12771.

710 **Lancaster, N.** (2020) On the formation of desert loess. *Quaternary Research*, **96**, 105-
711 122.

712 **Lancaster, N., Yang, X. and Thomas, D.** (2013) Spatial and temporal complexity in
713 Quaternary desert datasets: implications for interpreting past dryland dynamics and
714 understanding potential future changes. *Quaternary Science Reviews*, **78**, 301-302.

715 **Li, J., Zhang, Y., Dong, S. and Johnston, S.T.** (2014) Cretaceous tectonic evolution
716 of South China: A preliminary synthesis. *Earth-Science Reviews*, **134**, 98-136.

717 **Li, J., Zhang, Y., Zhao, G., Johnston, S.T., Dong, S., Koppers, A., Miggins, D.P.,
718 Sun, H., Wang, W. and Xin, Y.** (2017) New insights into Phanerozoic tectonics of
719 South China: Early Paleozoic sinistral and Triassic dextral transpression in the east
720 Wuyishan and Chencai domains, NE Cathaysia. *Tectonics*, **36**, 819-853.

721 **Li, X. H.** (2000) Cretaceous magmatism and lithospheric extension in Southeast China.
722 *Journal of Asian Earth Sciences*, **18**, 293-305.

723 **Li, G., Wu, C., Rodríguez-López, J.P., Yi, H., Xia, G. and Wagleich, M.** (2018a)
724 Mid-Cretaceous aeolian desert systems in the Yunlong area of the Lanping Basin, China:
725 Implications for palaeoatmosphere dynamics and paleoclimatic change in East Asia.
726 *Sedimentary Geology*, **364**, 121-140.

727 **Li, Y., He, D., Li, D., Lu, R., Fan, C., Sun, Y. and Huang, H.** (2018b) Sedimentary
728 provenance constraints on the Jurassic to Cretaceous paleogeography of Sichuan Basin,
729 SW China. *Gondwana Research*, **60**, 15-33.

730 **Li, Z. X. and Li, X. H.** (2007) Formation of the 1300-km-wide intracontinental orogen
731 and postorogenic magmatic province in Mesozoic South China: A flat-slab subduction
732 model. *Geology*, **35**, 179-182.

733 **Lindholm, R.** (2012) *A practical approach to sedimentology*. Springer Science &
734 Business Media.

735 **Ludwig, K.R.** (2003) User's manual for isoplot 3.00, a geochronological toolkit for
736 microsoft excel. *Berkeley Geochronol. Cent. Spec. Publ.*, **4**, 25-32.

737 **Lugli, S., Dori, S.M. and Fontana, D.** (2007) Alluvial sand composition as a tool to
738 unravel late Quaternary sedimentation of the Modena Plain, northern Italy. In:
739 *Sedimentary Provenance and Petrogenesis: Perspectives from Petrography and*
740 *Geochemistry* (Eds Arribas, J., Critelli, S., Johnsson, M. J.), Geol. Soc. Am. Sp. Paper,
741 **420**, 57-72.

742 **Ma, Y., Chen, H. and Wang, G.** (2009) Sequence stratigraphy and paleogeography in
743 South China. *Science Press, Beijing*.

744 **Maas, R., Kinny, P.D., Williams, I.S., Froude, D.O. and Compston, W.** (1992) The
745 Earth's oldest known crust: A geochronological and geochemical study of 3900–4200
746 Ma old detrital zircons from Mt. Narryer and Jack Hills, Western Australia. *Geochimica*
747 *et Cosmochimica Acta*, **56**, 1281-1300.

748 **Mountney, N.P.** (2006) Eolian facies models. In: *Facies Models Revisited* (Ed R.G.W.
749 H.W. Posamentier), **Special Publication**, pp. 19-83. Society for Economic
750 Paleontologists and Mineralogists, Tulsa, Oklahoma.

751 **Mu, H., Yan, D.-P., Qiu, L., Yang, W.-X., Kong, R.-Y., Gong, L.-X. and Li, S.** (2019)

752 Formation of the Late Triassic western Sichuan foreland basin of the Qinling Orogenic
753 Belt, SW China: Sedimentary and geochronological constraints from the Xujiache
754 Formation. *Journal of Asian Earth Sciences*, **183**, 103938.

755 **Muhs, D.R.** (2004) Mineralogical maturity in dunefields of North America, Africa and
756 Australia. *Geomorphology*, **59**, 247-269.

757 **Muhs, D.R., Lancaster, N. and Skipp, G.L.** (2017) A complex origin for the Kelso
758 Dunes, Mojave National Preserve, California, USA: A case study using a simple
759 geochemical method with global applications. *Geomorphology*, **276**, 222-243.

760 **O'Brien, C.L., Robinson, S.A., Pancost, R.D., Sinninghe Damsté, J.S., Schouten,**
761 **S., Lunt, D.J., Alsenz, H., Bornemann, A., Bottini, C., Brassell, S.C., Farnsworth,**
762 **A., Forster, A., Huber, B.T., Inglis, G.N., Jenkyns, H.C., Linnert, C., Littler, K.,**
763 **Markwick, P., McAnena, A., Mutterlose, J., Naafs, B.D.A., Püttmann, W., Sluijs,**
764 **A., van Helmond, N.A.G.M., Vellekoop, J., Wagner, T. and Wrobel, N.E.** (2017)
765 Cretaceous sea-surface temperature evolution: Constraints from TEX86 and planktonic
766 foraminiferal oxygen isotopes. *Earth-Science Reviews*, **172**, 224-247.

767 **Pastore, G., Baird, T., Vermeesch, P., Bristow, C., Resentini, A. and Garzanti, E.**
768 (2021) Provenance and recycling of Sahara Desert sand. *Earth-Science Reviews*, **216**,
769 103606.

770 **Qi, L., Hou, M., Cawood, P.A., Lang, X., Zhu, S. and Zhang, M.** (2023)
771 Neoproterozoic storm deposits in western Yangtze: Implications for the sea conditions
772 during the middle Sturtian glaciation. *Precambrian Research*, **384**, 106945.

773 **Rittner, M., Vermeesch, P., Carter, A., Bird, A., Stevens, T., Garzanti, E., Andò, S.,**

774 **Vezzoli, G., Dutt, R., Xu, Z. and Lu, H.** (2016) The provenance of Taklamakan desert
775 sand. *Earth and Planetary Science Letters*, **437**, 127-137.

776 **Rodríguez-López, J.P., Clemmensen, L.B., Lancaster, N., Mountney, N.P. and**
777 **Veiga, G.D.** (2014) Archean to Recent aeolian sand systems and their sedimentary
778 record: Current understanding and future prospects. *Sedimentology*, **61**, 1487-1534.

779 **Schiemann, R., Lüthi, D. and Schär, C.** (2009) Seasonality and interannual variability
780 of the westerly jet in the Tibetan Plateau region. *Journal of Climate*, **22**, 2940-2957.

781 **Shen, C., Donelick, R.A., O'Sullivan, P.B., Jonckheere, R., Yang, Z., She, Z., Miu,**
782 **X. and Ge, X.** (2012) Provenance and hinterland exhumation from LA-ICP-MS zircon
783 U–Pb and fission-track double dating of Cretaceous sediments in the Jiangnan Basin,
784 Yangtze block, central China. *Sedimentary Geology*, **281**, 194-207.

785 **Shu, L.S., Zhou, X.M., Deng, P., Wang, B., Jiang, S.Y., Yu, J.H. and Zhao, X.X.**
786 (2009) Mesozoic tectonic evolution of the Southeast China Block: New insights from
787 basin analysis. *Journal of Asian Earth Sciences*, **34**, 376-391.

788 **Tsoar, H. and Pye, K.** (1987) Dust transport and the question of desert loess formation.
789 *Sedimentology*, **34**, 139-153.

790 **Walker, J.D., Martin, M.W., Glazner, A.F. and Bartley, J.M.** (2002) Late Paleozoic
791 to Mesozoic development of the Mojave Desert and environs, California. In: *Geologic*
792 *Evolution of the Mojave Desert and Southwestern Basin and Range* (Eds Glazner A.F.,
793 Walker J.D., Bartley J.M.), Geological Society of America Memoir, **195**, 1-18.

794 **Wang, B. Q., Wang, W., Chen, W.T., Gao, J. F., Zhao, X. F., Yan, D. P. and Zhou,**
795 **M. F.** (2013) Constraints of detrital zircon U–Pb ages and Hf isotopes on the

796 provenance of the Triassic Yidun Group and tectonic evolution of the Yidun Terrane,
797 Eastern Tibet. *Sedimentary Geology*, **289**, 74-98.

798 **Wang, D. and Shu, L.** (2012) Late Mesozoic basin and range tectonics and related
799 magmatism in Southeast China. *Geoscience Frontiers*, **3**, 109-124.

800 **Wang, W. and Zhou, M.-F.** (2012) Sedimentary records of the Yangtze Block (South
801 China) and their correlation with equivalent Neoproterozoic sequences on adjacent
802 continents. *Sedimentary Geology*, **265-266**, 126-142.

803 **Wang, Y., Fan, W., Zhao, G., Ji, S. and Peng, T.** (2007) Zircon U–Pb geochronology
804 of gneissic rocks in the Yunkai massif and its implications on the Caledonian event in
805 the South China Block. *Gondwana Research*, **12**, 404-416.

806 **Whitford, W.G. and Duval, B.D.** (2019) *Ecology of desert systems*. Academic Press.

807 **Williams, M.** (2015) Interactions between fluvial and eolian geomorphic systems and
808 processes: Examples from the Sahara and Australia. *CATENA*, **134**, 4-13.

809 **Wu, C., Liu, C., Haisheng, Y., Xia, G., Zhang, H., Wang, L., Li, G. and Wagreich,**
810 **M.** (2017) Mid-Cretaceous desert system in the Simao Basin, southwestern China, and
811 its implications for sea-level change during a greenhouse climate. *Palaeogeography,*
812 *Palaeoclimatology, Palaeoecology*, **468**, 529-544.

813 **Wu, C., Rodríguez-López, J.P., Liu, C., Sun, X., Wang, J., Xia, G. and Wagreich,**
814 **M.** (2018a) Late Cretaceous climbing erg systems in western Xinjiang Basin.
815 Palaeoatmosphere dynamics and East Asia margin tectonic forcing on desert expansion
816 and preservation. *Marine and Petroleum Geology*, **93**, 539-552.

817 **Wu, H., Zhang, L., Gao, J., Zhang, M., Zhu, M. and Xiang, P.** (2018b) U–Pb

818 geochronology, isotope systematics, and geochemical characteristics of the Triassic
819 Dasuji porphyry Mo deposit, Inner Mongolia, North China: Implications for tectonic
820 evolution and constraints on the origin of ore-related granitoids. *Journal of Asian Earth*
821 *Sciences*, **165**, 132-144.

822 **Xi, D., Wan, X., Li, G. and Li, G.** (2019) Cretaceous integrative stratigraphy and
823 timescale of China. *Science China Earth Sciences*, **62**, 256-286.

824 **Yan, Y., Hu, X.-q., Lin, G., Santosh, M. and Chan, L.-S.** (2011) Sedimentary
825 provenance of the Hengyang and Mayang basins, SE China, and implications for the
826 Mesozoic topographic change in South China Craton: Evidence from detrital zircon
827 geochronology. *Journal of Asian Earth Sciences*, **41**, 494-503.

828 **Yu, X., Liu, C., Wang, C., Li, F. and Wang, J.** (2020) Eolian deposits of the northern
829 margin of the South China (Jiangnan Basin): Reconstruction of the Late Cretaceous
830 East Asian landscape in central China. *Marine and Petroleum Geology*, **117**, 104390.

831 **Yu, X., Liu, C., Wang, C. and Wang, J.** (2021a) Late Cretaceous aeolian desert system
832 within the Mesozoic fold belt of South China: Palaeoclimatic changes and tectonic
833 forcing of East Asian erg development and preservation. *Palaeogeography,*
834 *Palaeoclimatology, Palaeoecology*, **567**, 110299.

835 **Yu, X., Wang, C., Bertolini, G., Liu, C. and Wang, J.** (2021b) Damp- to dry aeolian
836 systems: Sedimentology, climate forcing, and aeolian accumulation in the Late
837 Cretaceous Liyou Basin, South China. *Sedimentary Geology*, **426**, 106030.

838 **Zhang, C., Li, Z., Chen, Q., Dong, S., Yu, X. and Yu, Q.** (2020) Provenance of eolian
839 sands in the Ulan Buh Desert, northwestern China, revealed by heavy mineral

840 assemblages. *CATENA*, **193**, 104624.

841 **Zhu, B., Yu, J., Qin, X., Rioual, P., Liu, Z. and Xiong, H.** (2014) Formation and
842 evolution of sand deserts in Xinjiang, Northwest China: I. Provenances of desert sands.
843 *Journal of Geographical Sciences*, **24**, 177-190.

844

845

846 **FIGURE CAPTIONS**

847 Fig. 1. (A) Sketch map showing the location of South China, modified after Li et al.
848 (2017). (B) Simplified geological map of South China delineating the distributions of
849 the Archean-Cretaceous strata and igneous rocks. Modified after Li et al. (2017). (C)
850 Geological and palaeogeographic map of the Xinjiang Basin. Blue circles represent
851 sampling sites and black-rimmed circles represent detrital zircon samples.

852

853 Fig. 2. The Cretaceous strata in the Xinjiang Basin. In the fourth column, according to
854 Li et al. (2019), the Hekou, Tangbian, and Lianhe formations were deposited coevally.
855 The Hekou and Lianhe formations represent the same lithostratigraphic unit in different
856 geographic locations. These formations predominately comprise gravel facies of flood
857 origin accumulated at the foot of mountains in the southern and northern margins of the
858 Xinjiang Basin. Basinwards, these alluvial facies gradually transition to aeolian facies
859 of the Tangbian Formation. Fm. = Formation and Gr. = Group.

860

861 Fig. 3. Thin-section photo-micrography of (A) alluvial sediments, (B) fluvial
862 sediments, (C) aeolian sediments from the desert-centre setting, and (D) aeolian
863 sediments from the desert-margin setting. (E) Q-F-L ternary diagram based on Garzanti
864 et al. (2019). Q = quartzose, Qs = single-crystal quartz, Qp = polycrystal quartz, F =
865 feldspathic, L = lithic, Ls = sedimentary lithics, lFQ = litho-feldspatho-quartzose, lQF
866 = litho-quartzo-feldspathic, qLF = quartzo-lithofeldspathic, qFL = quartzo-feldspatho-
867 lithic, fQL = feldspatho-quartzo-lithic, and fLQ = feldspatho-litho-quartzose.

868

869 Fig. 4. Cathodoluminescence (CL) images of representative zircon grains from the
870 Xinjiang intermountain desert. The small white circles show the sites for U–Pb age
871 analyses and the ages (Ma). YT-03 & YT-08 were taken from aeolian sediments in the
872 desert-centre setting; YT-07 & YT-13 were taken from aeolian sediments in the desert-
873 margin setting; YT-12 & YT-14 were taken from the alluvial-fluvial sediments.

874

875 Fig. 5. U–Pb concordia diagrams and normalized probability density distributions (blue
876 curves).

877

878 Fig. 6. Bar graph shows percentages of age populations (Ma) for each sample.

879

880 Fig. 7. Zircon U–Pb age probability density plots of the Mid-Late Cretaceous sediments
881 in the Xinjiang intermountain desert and potential source regions. All zircon ages show
882 discordance <10%. The zircon ages are divided into seven population groups: 98-217

883 Ma, 220-323 Ma, 328-482 Ma, 503-722 Ma, 732-1386 Ma, 1426-2174 Ma, and 2210-
884 2701 Ma. JNO—Jiangnan Orogen, YB-Yangtze Block, CB—Cathaysia Block,
885 SCMB—South China Magmatic Belt, W-YB—Western margin of Yangtze Block,
886 SJO—Sanjiang Orogen, SGT—Songpan-Ganzi terrane, NQB—North Qinling Belt,
887 SQB—South Qinling Belt, and S-NCB—Southern margin of the North China Block.
888 Data: JNO, W-YB, SJO, SGT, NQB, SQB, S-NCB derived from Li et al. (2018), YB
889 derived from Jian et al. (2019), CB derived from Mu et al. (2019), and SCMB derived
890 from Yan et al. (2011).

891

892 Fig. 8. Palaeogeographic map of southern China during the Mid-Late Cretaceous.
893 Modified after Wang (1985) and Ma et al. (2009). The mid-Cretaceous intermontane
894 desert in the Xinjiang Basin was mainly controlled by westerlies (green arrows). The
895 reconstructed palaeowind direction was toward the ENE. Since the South China Block
896 rotated by $16.7 \pm 5.0^\circ$ during mid-Cretaceous to Paleogene, so the palaeowind direction
897 depicted on the modern map is nearly directly eastward. SC—Sichuan Basin, JB—
898 Jiangnan Basin, CL—Chaling Basin, XJ—Xinjiang Basin, and SB—Subei Basin.

899

900 **TABLE CAPTIONS**

901 Table 1. Maximum depositional ages calculated from zircon U-Pb geochronology of
902 sandstone samples from the Xinjiang Basin

903

904 **SUPPORTING INFORMATION**

905 S1. Reconstruction of palaeowind directions for the Late Cretaceous Xinjiang
906 intermontane desert.

907

908 Fig. S1. Outcrops and line drawings of (A) small-scale barchan dunes, (B) large-scale
909 compound transverse dunes and (C) large-scale complex dunes. Black lines represent
910 aeolian surfaces (interdune migration surfaces, superimposition surfaces, and
911 reactivation surfaces); and gray, dashed lines represent cross-stratification. The
912 numbers before each arrow/after each arrow represent the azimuth/dip of the cross
913 beddings. Modified from Cao et al., 2020.

914

915 Fig. S2. Palaeogeographic map and palaeowind directions of the Tangbian Formation
916 in the Xinjiang Basin during the Late Cretaceous. Modified from Cao et al., 2020.

917

918 Fig. S3. Crossplot of Th/U ratios versus U–Pb ages of concordant detrital zircons from
919 sandstones in the Xinjiang intermontane desert.

920

921 Fig. S4. Cathodoluminescence (CL) images of representative 503-722 Ma zircon grains
922 from the Xinjiang intermontane desert. The small white circles show the sites for U–Pb
923 age analyses and the ages (Ma). YT-08 was taken from aeolian sediments in the desert
924 center, and YT-07 & YT-13 were taken from aeolian sediments in the desert margin.

925

926 Table S1. Location information of 14 sandstone samples throughout the Xinjiang Basin.

927

928 Table S2. Laser ablation inductively coupled plasma spectrometry (LA-ICP-MS) data
929 of detrital zircons from the Xinjiang intermontane desert in SE China.

Figure 1

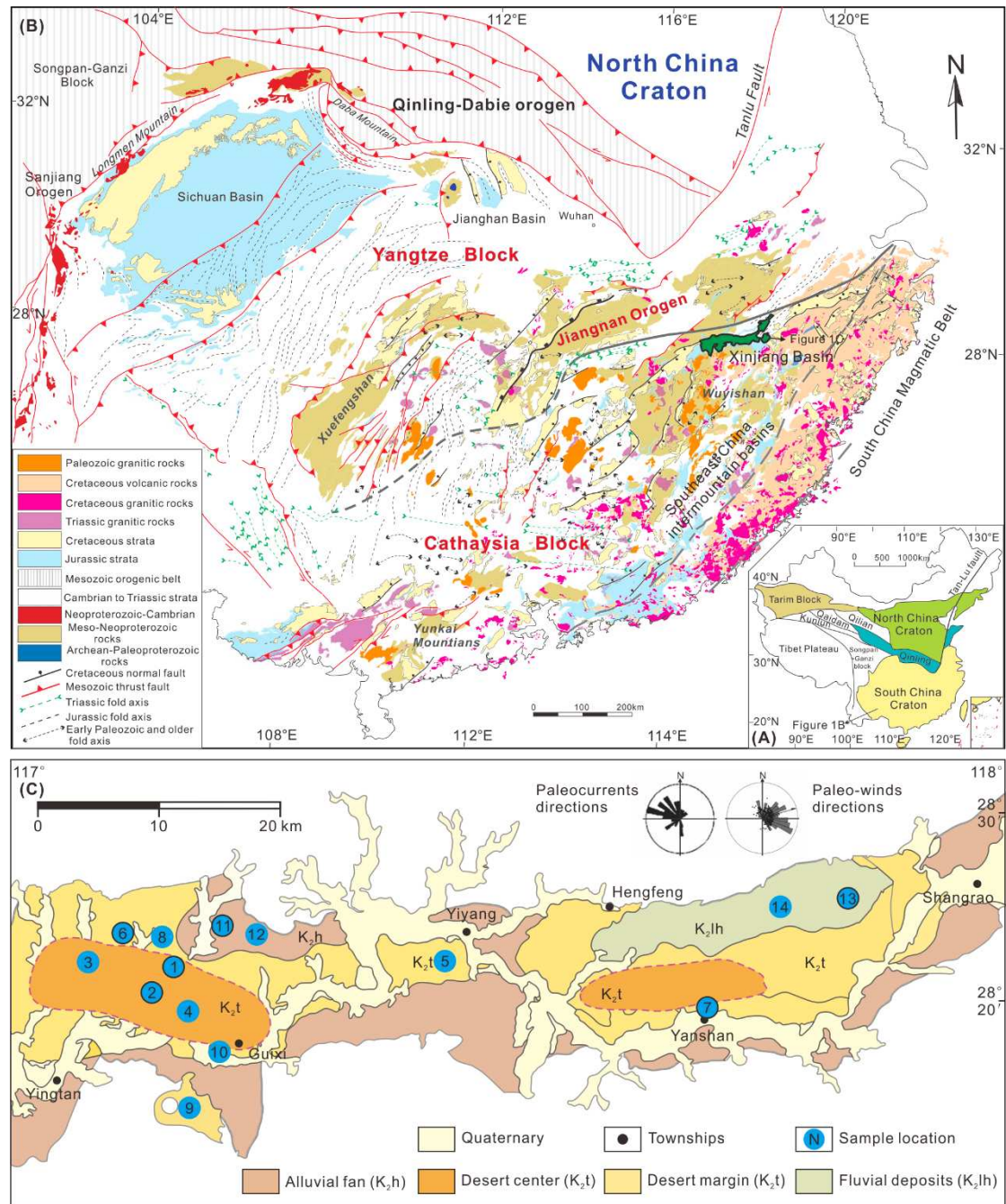


Figure 2

Series	Stage	Xi et al. (2019)	Li et al. (2019)	Facies and Brief Discription
Late Cretaceous	Maastrichtian	Guifeng Gr. Lianhe Fm. Tangbian Fm. Hekou Fm.	Lianhe Fm. Tangbian Fm. Lianhe Fm.	Guifeng Gr.: Lianhe Fm. (K ₂ lh)--Alluvial fan and braided stream, purple red sandy conglomerate and sandstone; Tangbian Fm.(K ₂ t)--Erg deposits, brick red sandstones; Hekou Fm.(K ₂ h)--Alluvial fan, purple red conglomerate and sandy conglomerate.
	Campanian			
	Santonian			
	Coniacian	Hekou Fm.	Lianhe Fm.	
	Turonian	Tangbian Fm.	Tangbian Fm.	
	Cenomanian	Hekou Fm.	Hekou Fm.	
Early Cretaceous	Albian	Zhoutian Fm.	Huobashan Gr.	Zhoutian Fm.(K ₂ z)--Playa, red sandstone with gypsum; Maodian Fm. (K ₂ m)--Alluvial fan and braided stream, conglomerate and sandy conglomerate. Huobashan Gr.: Volcanic depression, tuff and volcanic breccia with conglomerate.
		Maodian Fm.		
	Aptian	Lengshuiwu Fm.		

Figure 3

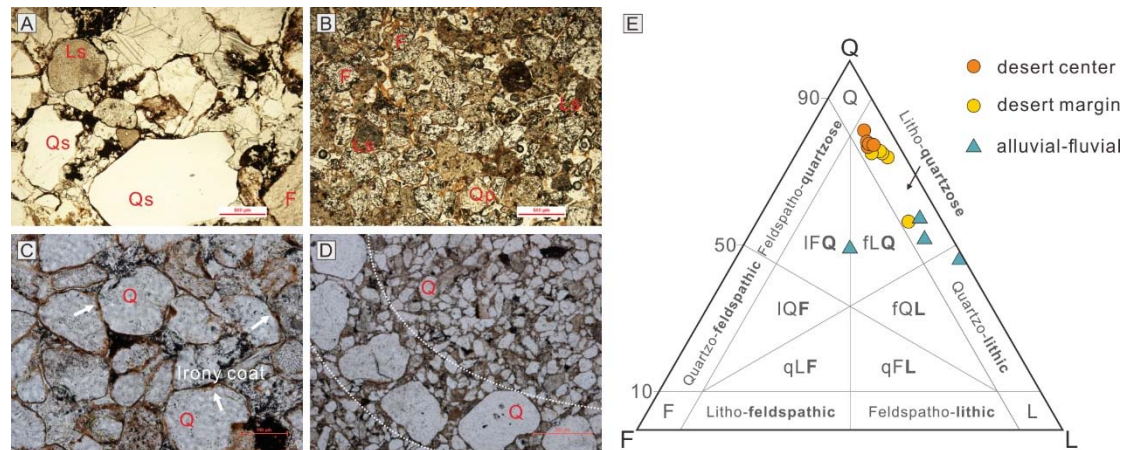


Figure 4



Figure 5

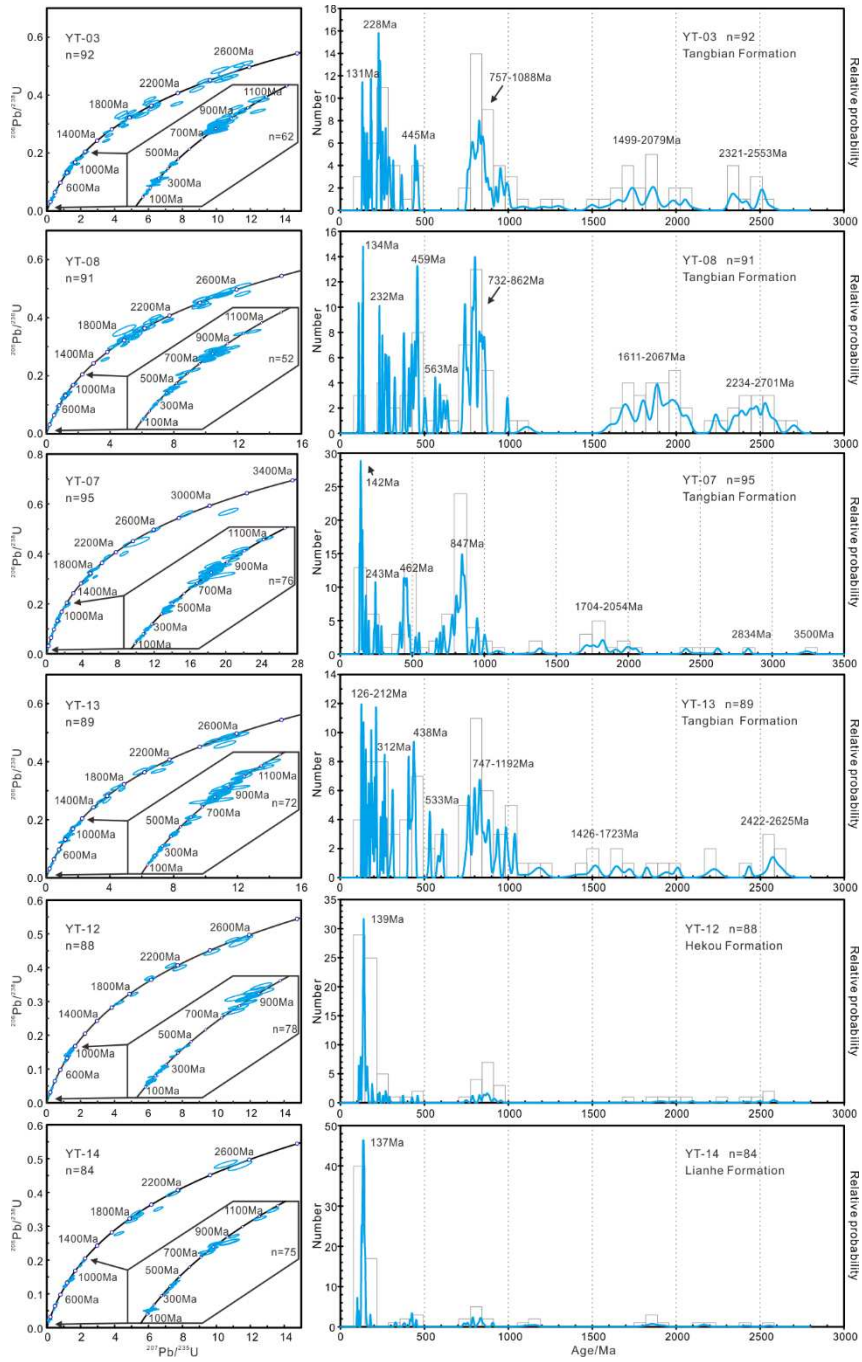


Figure 6

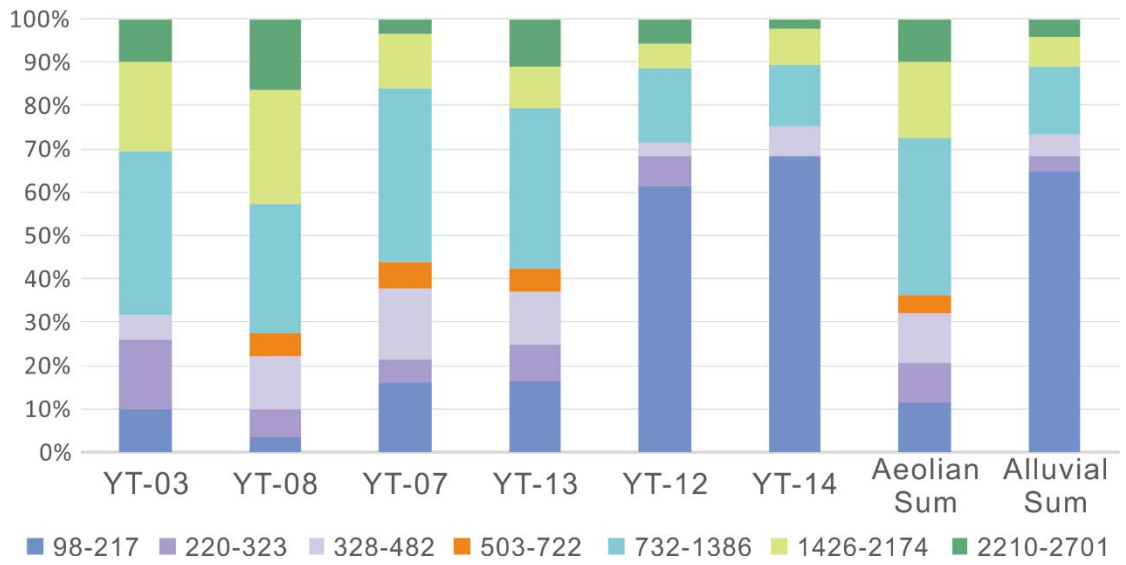


Figure 7

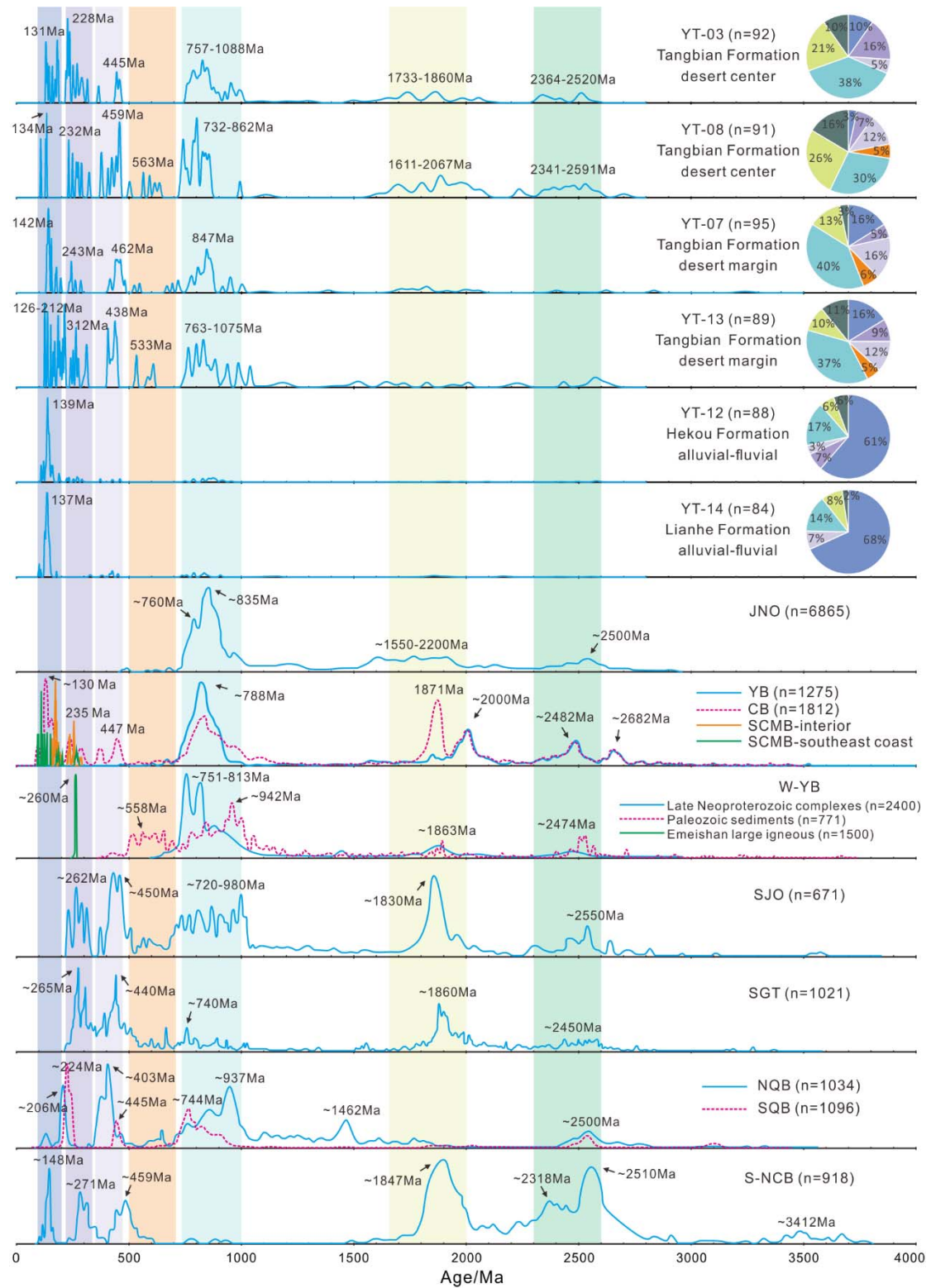


Figure 8

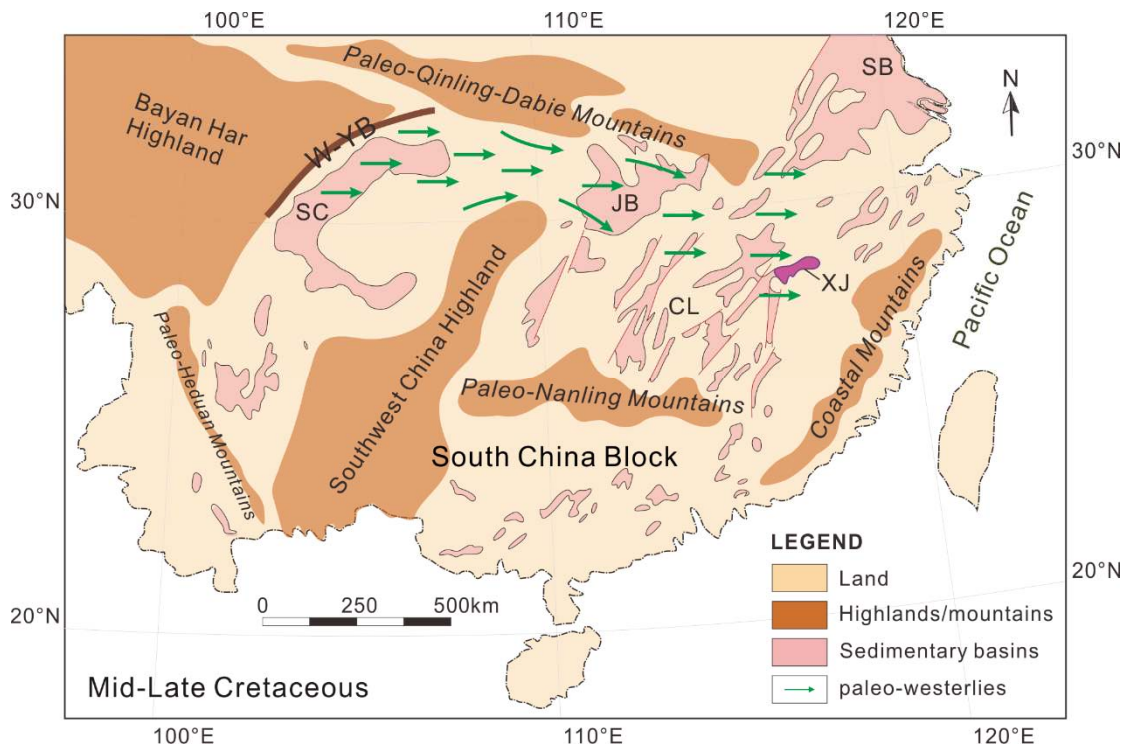


Table 1. Maximum depositional ages calculated from zircon U-Pb geochronology of sandstone samples from the Xinjiang Basin

Formation	Sample	Analyzed number of zircon grains	Maximum depositional age [*]	YDZ [†] (Ma)	YSG [†] (Ma)	YPP [†] (Ma)	YC1 σ (2+) [†] (Ma)	YC2 σ (3+) [†] (Ma)
K ₂ hl	YT-14	84	99.5	99+4.2/-10	98±4	100.8	99.5±3 (n=2)	102.3±3 (n=3)
	YT-03	92	131	129.6+4.8/-6.4	130±3	131.3	131±3 (n=2)	127±3 (n=3)
K ₂ t	YT-07	95	137	133.1+4.2/-9.8	134±3	141.8	137±4.3 (n=4)	140.2±3.8 (n=9)
	YT-08	91	132	108.3+6.3/-7.1	108±3	130.2	132±2.5 (n=2)	131.7±2.7 (n=3)
	YT-13	89	126	124.3+4.2/-4.5	125±2	126	126±2.5 (n=2)	129.7±2.7 (n=3)
K ₂ h	YT-12	88	109.5	108.5+3.3/-4.2	109±2	109.2	109.5±2 (n=2)	111.3±2 (n=3)

Note. *Maximum depositional age is determined by YC1 σ (2+). [†]Different measures of youngest detrital zircon age after Dickinson and Gehrels (2009). YDZ—age calculated by the “youngest detrital zircon” routine of isoplot (Ludwig, 2008); YSG—youngest single detrital zircon age with 1 σ uncertainty; YPP—youngest graphical detrital zircon age peak on an age-probability plot or age-distribution curve; YC1 σ (2+)—weighted mean age of two or more youngest grain ages overlapping in age at 1 σ ; YC2 σ (3+)—weighted mean age of three or more youngest grain ages overlapping in age at 2 σ .

1 SUPPORTING INFORMATION

2 Appendix S1

3 Reconstruction of Palaeowind Directions for the Late Cretaceous Xinjiang 4 Intermontane Desert

5

6 The aeolian sandstone with high-angle cross-bedding can be used as a proxy to
7 reconstruct palaeowind direction (Jiang, 2018). The relationships between dune types
8 and dominant directions of the effective winds are different. The mean cross-bed dip
9 directions of barchan, barchanoid, and transverse dunes are parallel to the wind
10 direction, especially the perfectly transverse dunes (Rubin and Carter, 2006). However,
11 the cross-beds dip directions of oblique and longitudinal dunes are not parallel to the
12 wind direction (Mountney, 2006; Rubin and Hunter, 1985). Rubin (1987) and Rubin
13 and Carter (2006) presented a collection of computer-generated images of cross-
14 bedding to distinguish the deposits of transverse, oblique and longitudinal bedforms.
15 For the perfectly transverse dunes, dips have bilateral symmetry and dip directions of
16 their cross-beds are distributed unimodally; for the oblique dunes, cross-bed dips are
17 asymmetrically distributed; for the perfectly longitudinal dunes, dips have bilateral
18 symmetry and dip directions of their cross-beds are often distributed bimodal (Rubin
19 and Carter, 1987; Rubin and Carter, 2006).

20 In the Late Cretaceous Xinjiang intermontane desert, the azimuths of aeolian dune
21 cross-beds were measured from 16 sections (Cao et al., 2020). As the South China
22 Block rotated by $16.7 \pm 5.0^\circ$ in the mid-Cretaceous to Paleogene, these measured data

23 have been corrected to the palaeo-direction. Sections 1, 3, 15, 16 are small-scale
24 barchan dunes (Fig. S1A). Consisting of high-angle trough cross beddings, they are
25 often less than 2 m in thickness and could be traced for only tens of meters in all
26 directions. They are much smaller than the large-scale aeolian dunes and the dip
27 directions of the cross-beds are variable (Fig. S2), which might be affected by the
28 secondary winds, so that they are excluded from the reconstruction of the primary
29 palaeowind direction. Their trough cross beddings have scoured bases and either
30 symmetrical or asymmetrical axes. Sections 5, 9, 11, 12 are large-scale near-perfectly
31 transverse dunes (Fig. S1B), parallel stacked and bounded by laterally extensive, very
32 low-angle inclined bounding surfaces. Generally, the thickness is tens of meters, and
33 their lateral distribution is several hundred meters. The compound forms are important
34 components of the draa bedform and distributed only in the central desert. The dip
35 directions of the cross-beds of these transverse dunes are consistent and unidirectional,
36 orienting to ENE, which are parallel to the palaeowind (Fig. S2). Sections 2, 8, 13 are
37 the large-scale longitudinal dunes. The dip directions of their cross-beds are in almost
38 opposite directions (Fig. S2). Sections 4, 6, 7, 10, 14 are the large-scale complex aeolian
39 dunes. They are a mix of transverse, oblique and longitudinal dunes. The dip directions
40 of their cross-beds are multi-directional, so that they can not accurately reflect the
41 palaeowind direction.

42 In conclusion, the large-scale near-perfectly transverse dunes are the ideal
43 materials for the reconstruction of palaeowind direction, and results shows that the
44 palaeowind blew from west-southwest to east-northeast, reflecting the influence of

45 westerlies.

46

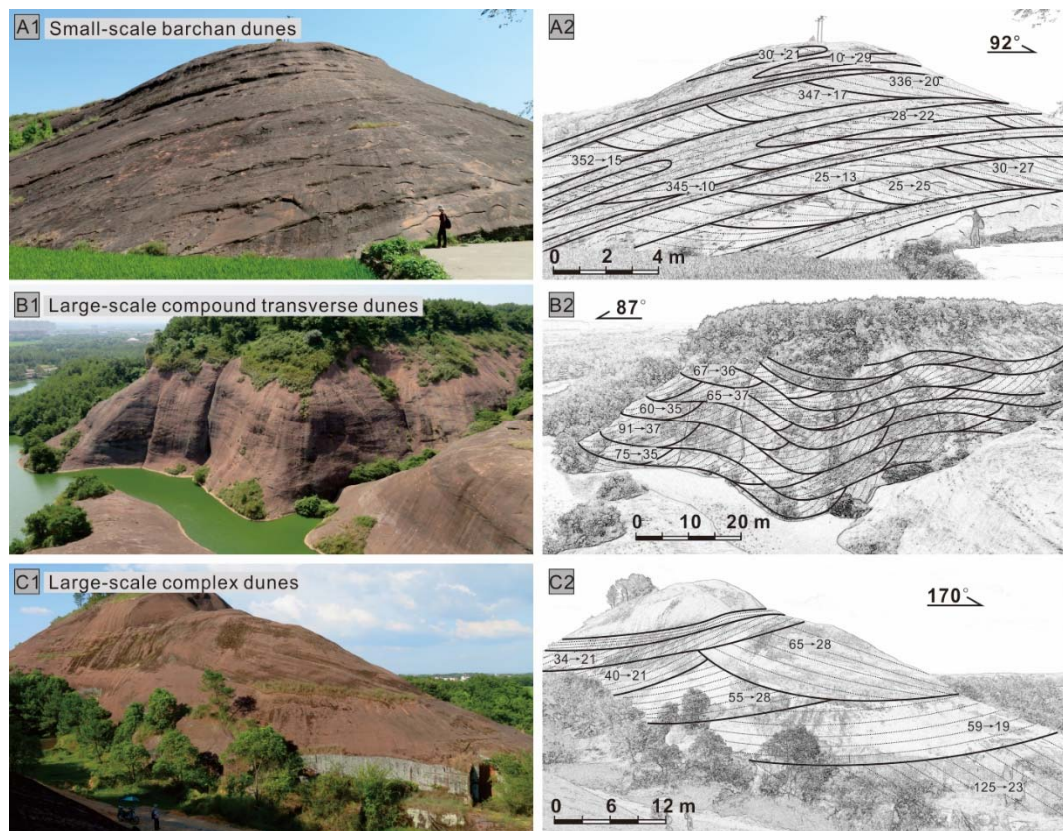


Fig. S1. Outcrops and line drawings of (A) small-scale barchan dunes, (B) large-scale compound transverse dunes and (C) large-scale complex dunes. Black lines represent aeolian surfaces (interdune migration surfaces, superimposition surfaces, and reactivation surfaces); and gray, dashed lines represent cross-stratification. The numbers before each arrow/after each arrow represent the azimuth/dip of the cross beddings. Modified from Cao et al., 2020.

47

48

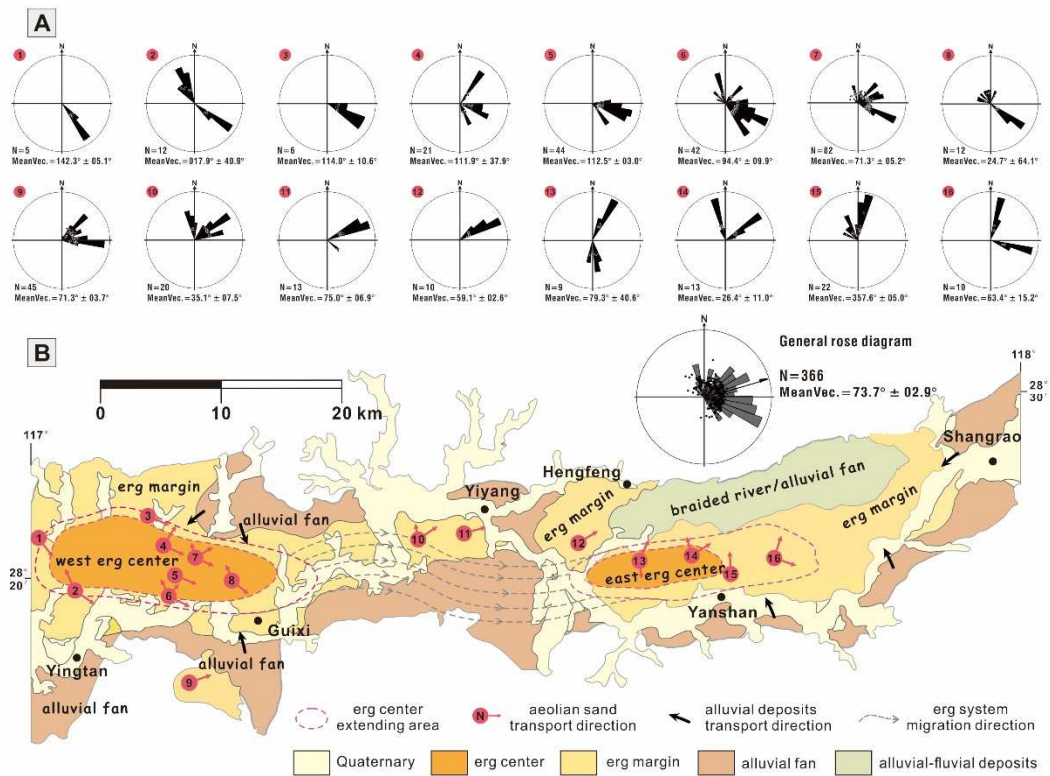


Fig. S2. Palaeogeographic map and palaeowind directions of the Tangbian Formation in the Xinjiang Basin during the Late Cretaceous. Modified from Cao et al., 2020.

49

50

51 **REFERENCES**

52 **Cao, S., Zhang, L., Wang, C., Ma, J., Tan, J. and Zhang, Z. (2020)** Sedimentological
 53 characteristics and aeolian architecture of a plausible intermountain erg system in
 54 Southeast China during the Late Cretaceous. *GSA Bulletin*, **132**, 2475-2488.

55 **Jiang, Z. (2018)** *Sedimentary dynamics of windfield-source-basin system: new concept*
 56 *for interpretation and prediction*. Springer.

57 **Mountney, N.P. (2006)** Eolian facies models. In: *Facies Models Revisited* (Ed R.G.W.
 58 H.W. Posamentier), **Special Publication**, pp. 19-83. Society for Economic
 59 Paleontologists and Mineralogists, Tulsa, Oklahoma.

60 Rubin, D.M. and Carter, C.L. (1987) *Cross-Bedding, Bedforms, and Paleocurrents*.

61 SEPM Society for Sedimentary Geology.

62 Rubin, D.M. and Carter, C.L. (2006) *Cross-bedding, bedforms, and paleocurrents*.

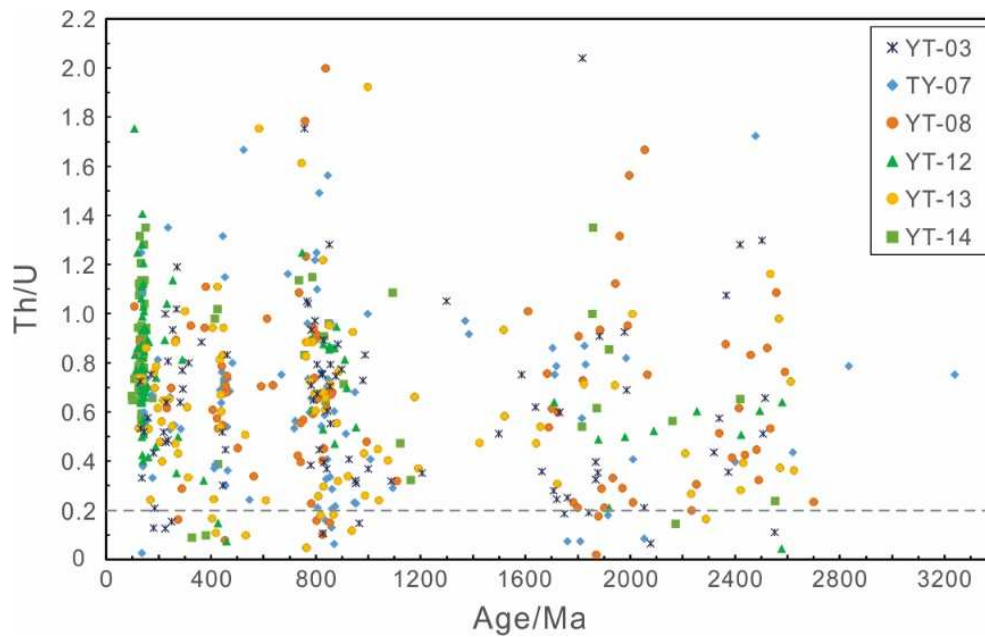
63 Society for Sedimentary Geology.

64 RUBIN, D.M. and HUNTER, R.E. (1985) Why deposits of longitudinal dunes are

65 rarely recognized in the geologic record. *Sedimentology*, **32**, 147-157.

66

67



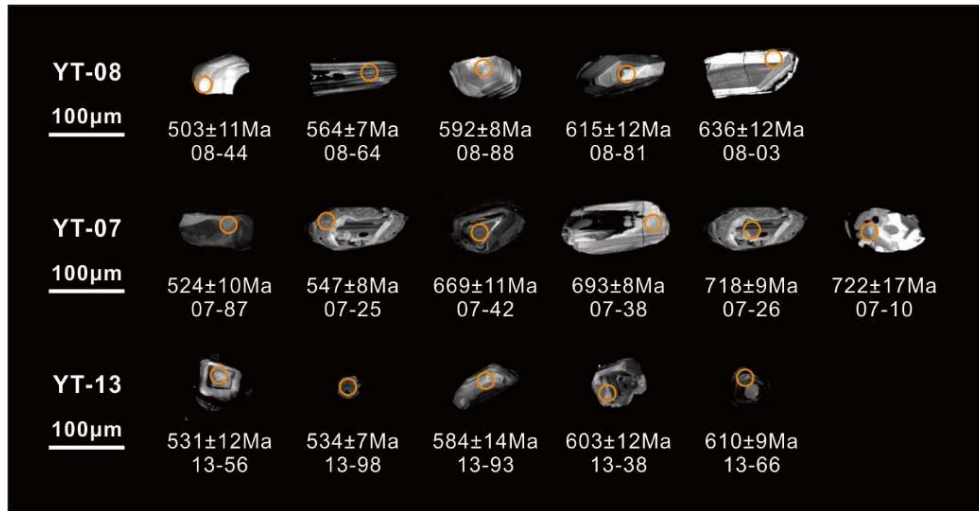
68

69 Fig. S3. Crossplot of Th/U ratios versus U–Pb ages of concordant detrital zircons from

70 sandstones in the Xinjiang intermountain desert.

71

72



73

74 Fig. S4. Cathodoluminescence (CL) images of representative 503-722 Ma zircon grains
 75 from the Xinjiang intermountain desert. The small white circles show the sites for U–
 76 Pb age analyses and the ages (Ma). YT-08 was taken from aeolian sediments in the
 77 desert center, and YT-07 & YT-13 were taken from aeolian sediments in the desert
 78 margin.

79

80

81 **Table S1.** Location information of 14 sandstone samples throughout the Xinjiang Basin.

No.	Sample	Formation	Section	Subregion	Type	GPS	Technique
1	YT-03	K _{2t}	Xianrenshi	Desert center	Barchan dune	28°21'54"N 117° 09'59"E	Thin section LA-ICP-MS
2	YT-08	K _{2t}	Longyanshan	Desert center	Transverse dune	28°20'29"N 117° 08'54"E	Thin section LA-ICP-MS
3	JXY-17	K _{2t}	Zhiguangzhen	Desert center	Transverse dune	28°22'10"N 117°04'39"E	Thin section
4	JXY-18	K _{2t}	Yanqianpengjia	Desert center	Transverse dune	28°17'57"N 117°10'40"E	Thin section
5	JXY-25	K _{2t}	Nanyansi	Desert center	Barchan dune	28°16'27"N 117°10'40"E	Thin section
6	YT-07	K _{2t}	Hejiacun	Desert margin	Dry interdune	28°23'34"N; 117° 08'19"E	Thin section LA-ICP-MS
7	YT-13	K _{2t}	Yanshan	Desert margin	Barchan dune	28°19'21"N 117°42'17"E	Thin section LA-ICP-MS

8	JXY-09	K ₂ t	Zhongcun	Desert margin	Dry Interdune	28°23'34"N 117°08'19"E	Thin section
9	JXY-15	K ₂ t	Hongshichang	Desert margin	Barchan dune	28°22'02"N 117°14'09"E	Thin section
10	JXY-21	K ₂ t	Yinlingshi	Desert margin	Sandsheet	28°16'54"N 117°12'23"E	Thin section
11	YT-12	K ₂ h	Houzhang	Extra desert	alluvial	28°24'07"N 117°12'53"E	Thin section LA-ICP-MS
12	JXY-22	K ₂ h	Zhujiayuan	Extra desert	alluvial	28°23'33"N 117°15'34"	Thin section
13	YT-14	K ₂ lh	Daguyan	Extra desert	Fluvial	28°25'33"N 117°51'08"E	Thin section LA-ICP-MS
14	JXS-02	K ₂ lh	Wanjiaozhu	Extra desert	Fluvial	E28°25'03"N 117°46'07"E	Thin section

82

83

84

85 Table S2. Laser ablation inductively coupled plasma spectrometry (LA-ICP-MS) data

86 of detrital zircons from the Xinjiang intermontane desert in SE China.

87